Quantifying Regional Efficiency of Marine Carbon Dioxide Removal (mCDR) via Alkalinity Enhancement using the ECCO-Darwin Ocean Biogeochemistry State Estimate and an Idealized Vertical 1-D Model

Kay Suselj[1], Dustin Carroll[2,1], Dimitris Menemenlis[1], Hong Zhang[1], Nate Beatty[3], Anna Savage[3], Daniel Whitt[4],

[1]Jet Propulsion Laboratory, California Institute of Technology, Pasadena, CA, USA
[2]Moss Landing Marine Laboratories, San José State University, Moss Landing, CA, USA
[3]Running Tide, Inc., Portland, ME, USA
[4]NASA Ames Research Center, Moffett Field, CA, USA

Key Points:

- We use a data-constrained ocean biogeochemistry model (ECCO-Darwin) to simulate regional Ocean Alkalinity Enhancement (OAE).
- OAE efficiency hinges on intricate ocean dynamics, air-sea gas exchange, and seasonality — components to consider for OAE deployment design.
- For computationally-efficient OAE optimization and quantification, we introduce and evaluate the performance of a reduced-complexity model.

Corresponding author: Kay Suselj, `kay.suselj@jpl.nasa.gov`

Abstract

As a marine Carbon Dioxide Removal (mCDR) approach, Ocean Alkalinity Enhancement (OAE) is emerging as a viable method for removing anthropogenic CO_2 emissions from the atmosphere to mitigate climate change. To achieve substantial carbon reduction using this method, OAE would need to be widespread and scaled-up across the global ocean. However, the efficiency of OAE varies substantially across a range of space-time scales and as such field deployments must be carefully planned to maximize efficiency and minimize logistical costs and risks. Here we develop a mCDR efficiency framework based on the data-assimilative ECCO-Darwin ocean biogeochemistry model, which examines two key factors over seasonal to multi-decadal timescales: 1) mCDR potential, which quantifies the CO_2 solubility of the upper ocean; and 2) dynamical mCDR efficiency, representing the full-depth impact of ocean advection, mixing, and air-sea CO_2 exchange. To isolate and quantify the factors that determine dynamical efficiency, we develop a reduced complexity 1-D model, rapid-mCDR, as a computationally-efficient tool for evaluation of mCDR efficiency. Combining the rapid-mCDR model with ECCO-Darwin allows for rapid characterization of OAE efficiency at any location globally. This research contributes to our understanding and optimization of OAE deployments (i.e., deploying experiments in the real-world ocean) as an effective mCDR strategy and elucidates the regional differences and mechanistic processes that impact mCDR efficiency. The modeling tools developed in this study can be readily employed by research teams and industry to plan and complement future field deployments and provide essential Monitoring, Reporting, and Verification (MRV).

Plain Language Summary

In an effort to counteract ongoing climate warming, engineering methods have been proposed to add materials to the ocean that increase the buffering capacity of seawater to sequester atmospheric carbon dioxide into the ocean — this is called Ocean Alkalinity Enhancement or OAE. However, expanding these pilot efforts to the scale where they would have a substantial impact on anthropogenic carbon emissions is a costly and challenging human endeavor. In order to simulate OAE deployments and guide future experiments and field trials, we used a state-of-the-art ocean model (ECCO-Darwin), which includes ocean carbon and biogeochemistry and is adjusted to be consistent with observations. We use both ECCO-Darwin and a reduced complexity model, which we develop

in this work, to show how and why the efficiency of OAE varies across ocean basins. Our modeling tools can be used by researchers and companies to better guide future OAE experiments in the real ocean.

1 Introduction

The major aim of the Paris Agreement is to reduce emissions and enhance carbon sinks that will keep the global temperature increase well below 2 degrees in this century (Rogelj et al., 2018; Schimel & Carroll, 2024). This limit requires a 50% reduction in anthropogenic carbon dioxide (CO_2) emissions by 2030, with emissions nearly eliminated by 2050 (i.e., net zero). This will require almost complete decarbonization of the world's energy supply (Friedlingstein et al., 2022; Palter et al., 2023). Furthermore, the IPCC's 6th assessment report has emphasized that atmospheric CO_2 removal on the gigaton scale will be necessary to reach net zero emissions (IPCC, 2022).

Due to the vast carbon reservoir size of the global ocean and its well-understood sink of anthropogenic CO_2 emissions (Gruber et al., 2019; Friedlingstein et al., 2022), various methods for marine carbon dioxide removal (mCDR) strategies have been proposed (National Academies of Sciences, Engineering, and Medicine, 2022). Ocean Alkalinity Enhancement (OAE; Renforth & Henderson, 2017) is a method designed to bolster the natural CO_2 absorption of the ocean. Examples of particular OAE approaches include: 1) removal of acidity through electrochemical processes (House et al., 2007), 2) deliberate deployment of alkaline substances on the surface ocean, and 3) enhanced weathering of alkaline minerals in the terrestrial environment or coastal zone (Taylor et al., 2016; Montserrat et al., 2017). Eisaman et al. (2023) provides a detailed technical review of various OAE approaches.

The core principle of OAE leverages tight coupling between ocean alkalinity (Alk) and the nonlinear marine carbonate chemistry system (Middelburg et al., 2020). OAE is generally focused on the deployment of near-surface Alk, which transforms aqueous carbon dioxide (CO_2) into bicarbonate (HCO_3^{2-}) and carbonate ions (CO_3^{2-}) ions through a series of rapid acid-base reactions (Zeebe & Wolf-Gladrow, 2001). This chemical adjustment leads to a reduction in aqueous CO_2 and thus lowers the partial pressure of carbon dioxide ($p$$CO_2$) in seawater. If the $p$$CO_2$ reduction occurs in the near-surface ocean, it can induce disequilibrium with atmospheric $p$$CO_2$ and drive ocean uptake of CO_2 from the atmosphere. This uptake acts to restore the ocean-atmosphere $p\mathrm{CO_2}$ gradient (i.e., the disequilibrium which resulted from OAE deployment) back towards an equilibrium state.

OAE is well established as a conceptual mechanism in marine geoengineering. Furthermore, National Academies of Sciences, Engineering, and Medicine (2022) ocean-based CDR research strategy plan states that OAE efficacy is rated as "high confidence", with durability and scalability as "medium-high", yet the knowledge base remains "low-to-medium". To permit widespread gigaton-scale OAE, it is critical to conduct field trials as these include aspects of ocean-atmosphere exchange, ocean-sediment exchange, biogeochemical side effects and feedbacks, and ecological dynamics that cannot be replicated with lab experiments (Iglesias-Rodríguez et al., 2023). With the rapid growth of start-up companies involved in mCDR, which are starting to market $\mathrm{CO_2}$ removal to buyers interested in offsetting carbon emissions, there is an urgent need to develop numerical tools to 1) simulate, optimize, and quantify efficiency of mCDR approaches at various ocean locations before expensive and labor-intensive field tests are conducted, 2) permit standardized third-party Monitoring, Reporting, and Verification (MRV) of the associated carbon capture, and 3) assess potential harmful impacts to aquatic and ocean ecosystems.

For typical ocean conditions, OAE has a potential to remove between 0.75 to 1 mole of $\mathrm{CO_2}$ from the atmosphere per mole of deployed Alk (Renforth & Henderson, 2017; Tyka et al., 2022). The actual amount, however, hinges on the complex interplay of ocean physics, thermodynamics, and biogeochemistry (Sarmiento & Gruber, 2006). While carbonate chemistry reactions can be assumed to occur nearly instantaneously, reequilibration of ocean $p\mathrm{CO_2}$ perturbations occur over annual-to-decadal timescales (Jones et al., 2014; He & Tyka, 2023). This reequilibration process takes place against the backdrop of multi-scale ocean dynamics, which influence the marine carbonate system state and can sequester disequilibrated waters away from the air-sea interface and deep into the ocean interior. Hence, as corroborated by prior numerical investigations (Ilyina et al., 2013; González et al., 2018; Burt et al., 2021; He & Tyka, 2023), the effectiveness of OAE is subject to considerable regional and temporal variability across the global ocean. However, the details of how the three-dimensional ocean circulation, sea-ice, carbonate, and ecological state impact regional OAE experiments through space and time have yet to be quantified using data-constrained ocean simulations.

In this study, we assess the effectiveness of OAE as a mCDR approach across various ocean regions representative of distinct dynamical and biogeochemical regimes. To achieve this, we utilize a new version of the ECCO-Darwin biogeochemistry model over the period from January 1995 to December 2017. The ECCO-Darwin model is particularly well-suited for simulating OAE as it assimilates a suite of in-situ and remotely-sensed physical and biogeochemical observations (Carroll et al., 2020, 2022) and thus provides the realistic background ocean state required for quantifying mCDR efficiency in the context of MRV (Köhler et al., 2013). As such, the ECCO-Darwin model accurately depicts the spatiotemporal evolution of historical ocean conditions, which typical climate models do not as they are not constrained by observations. Furthermore, unlike conventional assimilation techniques, the ECCO-Darwin data assimilation method avoids introducing non-physical source and sink terms (Carroll et al., 2022), making it an ideal tool for attributing OAE impacts on the time-dependent, three-dimensional ocean carbon, biogeochemical, and ecological state.

To achieve a computationally-efficient assessment of mCDR CO_2 uptake efficiency, we develop a reduced-complexity, vertically-resolved 1-D model termed *rapid-mCDR*. Rapid-mCDR simulates the vertical transport of dissolved inorganic carbon (DIC) and Alk perturbations and OAE additionality (i.e. net CO_2 uptake due to OAE). We demonstrate that rapid-mCDR can emulate key processes that affect mCDR additionality found in the higher-complexity 3-D ECCO-Darwin model. We use rapid-mCDR to expand our regional ECCO-Darwin analysis to basin-wide scales. Unlike ECCO-Darwin, which at present time needs to be run on a high-performance computing platform, rapid-mCDR can be easily run on a personal computer. We therefore propose that rapid-mCDR can serve as an alternative method for efficiently planning, characterizing, and optimizing field deployments, and thus can be used as the numerical foundation for MRV of mCDR deployments.

2 Methods

2.1 Quantification of OAE-driven Atmospheric CO_2 Removal

In this section, we summarize our approach for separating the impacts of dynamical and biogeochemical processes on OAE additionality (defined as the net CO_2 removed

Term/Symbol	Brief Explanation/Reference
Deployment site	Location of surface-ocean Alk injection.
OAE additionality	Net CO_2 removed from the atmosphere due to OAE (Section 2.1).
$mCDR_{pot}$	mCDR potential, i.e. maximum OAE additionality per unit of deployed Alk (Section 2.1).
$mCDR_{eff}$	Dynamical mCDR efficiency (Section 2.1).
$mCDR_{eff}^{cont}$	Dynamical mCDR efficiency for continuous OAE experiments (Equation 3).
$mCDR_{exch}$	Normalized net CO_2 flux (Supporting Information Text S2, Section 1).
$mCDR_{eff}^{sol}$	Solubility component of $mCDR_{eff}$ (Supporting Information Text S2, Section 3).
$mCDR_{equil}$	CO_2 Equilibration coefficient (Supporting Information Text S2, Section 4)
rapid-mCDR (Deploy)	Reduced-complexity rapid-mCDR model with input ocean conditions horizontally averaged over the deployment site (Section 4).
rapid-mCDR (HorAdv)	Rapid-mCDR model with input ocean conditions accounting for horizontal advection at the ocean surface (Section 4).

Table 1. List of key quantities used in this work.

from the atmosphere). Supporting Information Text S2–S4 describes these methods in further detail and Table 1 provide a list of key terms and symbols used in this work.

When Alk is deployed into the surface ocean at location a_0 with a time-dependent prescribed rate (i.e., flux integrated over a_0) of $f_{Alk}(t)$, the OAE-attributed CO_2 uptake can be written as the integral function:

$$\Delta F_{CO_2}(\tau) = \int_{t_s}^{\tau} f_{Alk}(t) \times mCDR_{pot}(t, a_0) \times mCDR_{eff}(\tau - t, t, a_0)\,\mathrm{d}t, \tag{1}$$

where ΔF_{CO_2} represents the total OAE additionality by time τ (in units of mol C), and $mCDR_{pot}$ and $mCDR_{eff}$ are mCDR potential and dynamic efficiency averaged over deployment site area a_0. Times t_s and τ denote, respectively, the start time of OAE deployment and time when the OAE additionality is evaluated. The integration period spans time $t = t_s$ to $t = \tau$.

The mCDR potential, $mCDR_{pot}(t, a_0)$, represents the maximum possible ocean CO_2 uptake per unit of Alk addition at time t and averaged over surface area a_0. It is computed assuming complete reequilibration of ocean $p$$CO_2$ and neglects any other feedbacks except disassociation of aqueous CO_2 bicarbonate and carbonate ions. The dynamical efficiency, $mCDR_{eff}(\tau{-}t, t, a_0)$, characterizes the fraction of mCDR potential that has been realized by time $\tau - t$ (for Alk deployed at time t over area a_0) and is primarily controlled by 3-D ocean dynamics and air-sea gas exchange.

Separation of OAE additionality into potential- and dynamical-efficiency components provides a meaningful separation into drivers relating to CO_2 solubility and ocean dynamics, respectively. This separation is accurate only when OAE additionality is linear with regards to the deployed Alk flux (i.e., the total amount of added Alk is small enough that it does not substantially impact $mCDR_{pot}$ and $mCDR_{eff}$) and the deployment site area a_0 is small enough that both $mCDR_{pot}$ and $mCDR_{eff}$ do not significantly vary across it.

As shown in previous work, $mCDR_{pot}$ values typically range between 0.75–1 mol C per mol Alk. $mCDR_{eff}$ is approximately an exponential function of elapsed time after OAE deployment with a characteristic multi-annual relaxation time, where over the multi-decadal time scales $mCDR_{eff}$ can reach values of up to one (e.g., He & Tyka, 2023).

For simplicity, in Equation 1 $mCDR_{pot}$ is defined as the average value over deployment site a_0 at deployment time t, whereas its value over the area and time where actual net OAE CO_2 exchange occurs is the relevant mCDR potential. In our framework, the difference between the two $mCDR_{pot}$ values is reflected in a modification of $mCDR_{eff}$. In Section 3.1, we show that $mCDR_{pot}$ values vary gradually with time and distance from the deployment site. Therefore, the impact of varying $mCDR_{pot}$ on $mCDR_{eff}$ are small.

Sections 2.1.1 and 2.1.2 describe methods for estimating $mCDR_{pot}$ and $mCDR_{eff}$ respectively, as they are the key factors that impact OAE additionality. If their global values are known, Equation 1 provides a framework for characterizing the OAE additionality of any deployment in the global ocean with a known Alk rate f_{Alk}.

2.1.1 Estimation of mCDR Potential, $mCDR_{pot}$

$mCDR_{pot}$ can be estimated diagnostically from surface-ocean thermodynamic and carbonate conditions using a marine carbonate chemistry solver (Follows et al., 2006). The results of the baseline/unperturbed ECCO-Darwin simulation, which are described in Section 2.2.1, provide all of the necessary inputs and we use the *PyCO2SYS* (Humphreys et al., 2022) Python toolbox for solving the marine carbonate chemistry system, as detailed in Supporting Information Text S3.

To estimate the reliability of $mCDR_{pot}$ from ECCO-Darwin, we also compute its values using the OceanSODA-ETHZ product (Gregor & Gruber, 2021). While we do not argue that $mCDR_{pot}$ from any of the two datasets is superior, our comparison shows broad-scale consistency, therefore lending support for the use of ECCO-Darwin to estimate $mCDR_{pot}$.

2.1.2 Estimation of mCDR Dynamical Efficiency ($mCDR_{eff}$): Pulse and Continuous OAE Experiments

At present time, the most obvious way of quantifying $mCDR_{eff}$ is by running numerical OAE experiments for locations and times of interest using global-ocean biogeochemistry models, such as ECCO-Darwin. An approach discussed in He and Tyka (2023) considers pulse experiments, where Alk is deployed over a short period (i.e., one month, which is short compared to CO_2 reequilibration timescales). For a pulse experiment, in which OAE is applied at time t and location a_0, the cumulative CO_2 flux at time τ can be expressed as:

$$\Delta F_{CO_2}(\tau) = \Delta Alk \times mCDR_{pot}(t, a_0) \times mCDR_{eff}(\tau - t, t, a_0) \tag{2}$$

Equation 2 can be derived from Equation 1, assuming that the Alk flux f_{Alk} follows a Dirac delta function with a spike at time t and a total Alk addition ΔAlk.

For the pulse experiments, $mCDR_{eff}$ is evaluated using Equation 2, where the cumulative OAE additionality is estimated from the difference in simulated CO_2 flux between OAE and baseline/unperturbed simulations. This approach can be computationally expensive if substantial regions of the global ocean over multiple deployment times (e.g., different seasons) are considered, as for each location (a_0) and deployment time (t) a new numerical experiment needs to be run. In fact, a single OAE simulation itself is computationally expensive because it needs to represent the large ocean volume (e.g., global ocean) that is potentially affected by OAE over the duration of a decade or longer — this is required to fully characterize the spread of OAE perturbations and long timescales associated with $mCDR_{eff}$.

While we find pulse experiments useful, here we propose a modified approach using a continuous OAE deployment as our primary method for characterization of OAE additionality. For a continuous OAE experiment starting at time t_s and with a constant OAE flux f_{Alk}, the instantaneous flux of CO_2, Δf_{CO_2} at time τ ($\tau > t_s$), can be expressed as (see Supporting Information Text S4 for details):

$$\Delta f_{CO_2}(\tau) = f_{Alk} \times \overline{mCDR_{pot}(a_0,t)}|_{t_s}^{\tau} \times mCDR_{eff}^{cont}(\tau - t_s, t_s, a_0), \tag{3}$$

where $\overline{mCDR_{pot}(a_0,t)}|_{t_s}^{\tau}$ represents the time-mean value of $mCDR_{pot}(a_0,t)$ from t_s to τ.

Equation 3 provides a definition for $mCDR_{eff}^{cont}$, which is closely related to $mCDR_{eff}$ as discussed below. Numerically, $mCDR_{eff}^{cont}$ is estimated by differencing CO_2 flux between the continuous OAE and baseline/unperturbed simulations, similar to how it is done for pulse experiments except that we compare the instantaneous instead of cumulative CO_2 flux.

The dynamical efficiencies for pulse and continuous OAE experiments are closely related (Supporting Information Text S4). $mCDR_{eff}^{cont}$, filtered with a high-frequency filter (for example, with an annual running-mean filter), represents time-mean values of $mCDR_{eff}$. Therefore, a single continuous OAE experiment can be used to characterize the time-mean mCDR efficiency for a certain location. The continuous OAE experiments also better characterizes overall OAE additionality of deployment sites. $mCDR_{eff}^{cont}$ also indicates variability of CO_2 uptake on a shorter timescales (e.g., seasonal). Note that the OAE-attributed CO_2 flux is proportional to $mCDR_{eff}^{cont}$. If such variability is identified to be considerable, it is likely that $mCDR_{eff}$ will be highly dependent on the time/season of OAE deployment, which can be further investigated using targeted pulse experiments.

In summary, our numerical studies rely primarily on continuous OAE experiments, which help us assess overall dynamical mCDR efficiency and pinpoint geographical areas with considerable short-term variability (e.g., seasonal). We find that mCDR efficiency for regions with significant seasonal variability depends on the deployment time and therefore requires supplementary pulse experiments to identify the dependence of $mCDR_{eff}$ on the deployment time/season.

2.2 ECCO-Darwin Experiments for Quantification of mCDR Potential and Dynamical Efficiency

2.2.1 ECCO-Darwin Description

The ECCO-Darwin model and data assimilation methods have been extensively described in the literature (e.g., Brix et al., 2015; Manizza et al., 2019, 2023; Carroll et al., 2020, 2022; Bertin et al., 2023). In particular, a technical description of the ECCO-Darwin model set-up, observational constraints, and optimization methodology is presented in Carroll et al. (2020). In this study, we use a coarser-resolution (1° vs 1/3° horizontal grid spacing) version of the Carroll et al. (2020) solution. Below, we provide a brief introduction to ECCO-Darwin and highlight the unique features of this model that are essential for our OAE studies.

The Lat-Lon-Cap-90 (LLC90) version of ECCO-Darwin used in this paper has 1° nominal horizontal grid spacing, spans 1992–2017, and is based on ocean circulation and physical tracers (i.e., temperature, salinity, and sea ice) from the Estimating the Circulation and Climate of the Ocean (ECCO) Version 4 release 4 solution (V4r4; ECCO Consortium, 2021; Forget et al., 2015). Horizontal grid spacing varies from 110 km at mid-latitudes to roughly 42 km at high latitudes. The vertical grid spacing increases from 10 m near the surface to 457 m near the seafloor. Since the horizontal discretization is insufficient to resolve mesoscale eddies, their impact on large-scale ocean circulation is parameterized using the Redi (1982) and Gent and McWilliams (1990) schemes; vertical mixing is parameterized with the Gaspar et al. (1990) scheme.

The ECCO V4r4 circulation estimate is used at each time step to drive an online biogeochemistry and ecosystem model developed by the Massachusetts Institute of Technology Darwin Project (Follows et al., 2007; Dutkiewicz et al., 2015, 2020). The Darwin model includes the cycling of organic and inorganic carbon, phosphorus, iron, silica, oxygen, and Alk. Carbonate chemistry is based on the efficient solver of Follows et al. (2006). Air-sea CO_2 flux is computed using the parameterization of Wanninkhof (1992) and forced with atmospheric partial pressure of CO_2 from the zonally-averaged National Oceanic and Atmospheric Administration Marine Boundary Layer Reference (NOAA MBL) product (Andrews et al., 2014). The Darwin ecology includes five large-to-small phytoplankton functional types (diatoms, other large eukaryotes, Synechococcus, and low- and high-light adapted Prochlorococcus), along with two zooplankton types that graze preferentially on either large eukaryotes or small picoplankton.

Physical observations are assimilated using the adjoint method (i.e., 4-D-Var; Wunsch et al., 2009; Wunsch & Heimbach, 2013), which minimizes a weighted least squares sum of model-data misfit (i.e., a cost function) to optimize initial conditions, time-varying surface-ocean boundary conditions, and time-invariant, three-dimensional mixing coefficients for along-isopycnal, cross-isopycnal, and isopycnal thickness diffusivity. Because the initial conditions, surface boundary conditions, and mixing coefficients are estimated as part of the adjoint-method optimization, the ECCO ocean circulation estimate has negligible drift and therefore does not require spin-up. The biogeochemical model is optimized in an additional step from the circulation using a low-dimensional Green's Functions approach (Menemenlis et al., 2005) to assimilate a variety of biogeochemical observations and adjust Darwin initial conditions and ecological parameters. We neglect the first 3 years of model simulation due to biogeochemical spin-up. The LLC90 ECCO-Darwin version closely matches the previously-published solution (Supporting Information Figure S2).

2.2.2 ECCO-Darwin OAE Experiments

We first ran an unperturbed *baseline* simulation that represents the natural state of the ocean in the absence of any OAE perturbations. The time period used in this analysis spans from January 1, 1995 to December 31, 2017. In Supporting Information Text S1, we show that the results of the *baseline* ECCO-Darwin simulation agree well with observations over the global surface ocean and in the various OAE deployment sites.

A suite of perturbed continuous and pulse OAE simulations were simulated, with Alk deployed at one of five deployment locations that are representative of diverse dynamical and biogeochemical open-ocean regions. The deployment locations are discussed in Section 2.2.5 and summarized in Table 2. The perturbed simulations were compared against the baseline simulation to evaluate the impact of OAE on the biogeochemical ocean state and OAE additionality. For the perturbed simulations, we do not consider a particular OAE approach in terms of materials used and its dissolution rate, etc., but simply assume deployment of Alk at a prescribed rate.

2.2.3 Continuous OAE Experiments

For *continuous OAE experiments*, a constant Alk flux is applied to the ECCO-Darwin surface-ocean layer (which is 10-m thick) over a regionally-defined deployment site from January 1995 to December 2017. Continuous experiments are performed for all five deployment locations described in Section 2.2.5. This allow us to estimate time-mean mCDR efficiency and its variability, which might be the most relevant factors characterizing field deployment locations.

For each of these experiments, an Alk rate (i.e., surface-integrated flux) of 3.33×10^7 mol eq. s^{-1} is applied over a horizontal area of roughly 270×10^3 km^2. The amount of deployed Alk is such that each experiment has a potential to remove 10^{-2} Pg C yr^{-1} from the atmosphere, assuming 0.8 mol of CO_2 is removed for each mole of deployed Alk. The molar ratio between removed CO_2 and added Alk is approximately valid for the global ocean and assumes complete reequilibration of ocean $p\mathrm{CO}_2$

citeHe2023. Its exact value varies regionally as discussed in Section 3.1; we use the ratio of 0.8 only as a rough estimate to contextualize the potential CO_2 uptake due to OAE. We expect that the results will be fairly insensitive to the horizontal deployment area, as long as it is large enough to avoid inorganic mineral precipitation.

We note that the magnitude of ocean CO_2 uptake, pH perturbations, and other possible environmental impacts, which will be specific to the particular OAE approach used (and might include inorganic mineral precipitation and impact on marine food web via the introduction of micro-nutrients and trace metals), are expected to be strongly correlated with the magnitude of the OAE Alk flux. In this work, we do not explore these environmental impacts in depth as they are specific to the particular OAE approach. As described in Section 2.1, our characterized OAE efficiency is normalized by Alk flux and is not sensitive to its exact value.

2.2.4 Pulse OAE Experiments

For two deployment sites associated with strong seasonality in $mCDR_{eff}^{cont}$ (North Atlantic Subduction (NAS) and Antarctic Circumpolar Current (ACC), see Section 2.2.5

and Table 2 for more details), we performed three additional types of pulse experiments with shorter Alk deployments. These experiments are used to further elucidate dependence of mCDR efficiency to deployment season.

For two *monthly-pulse* experiments, OAE is applied for a duration of 31 days, starting on January 1, 1995 and July 1, 1995; these monthly-pulse experiments are termed *Jan1995* and *Jul1995* experiments, respectively. The monthly-pulse experiments start during the months associated with nearly minimum and maximum $mCDR_{eff}^{cont}$. For these experiments, the magnitude of the Alk flux is such that each pulse experiments has a potential to remove 10^{-2} Pg C from the atmosphere (with the same assumption of molar ratio between added Alk and removed CO_2 as before).

For the *yearly-pulse* OAE experiments, Alk is deployed during a single year (from January 1st 1995 to December 31st 1995), where the magnitude of the Alk flux is equal to that of the monthly pulse experiments and therefore the potential removed CO_2 from the atmosphere is roughly 12 times larger compared to the monthly-pulse experiments. We refer to these experiments as *Yr1995* experiments. While the duration of the Alk pulse in the three pulse OAE experiments may appear long, we stress that its timescale is short compared to typical multi-year to decadal CO_2 reequilibration timescales (He & Tyka, 2023).

2.2.5 OAE Experiment Locations

Figure 1 and Table 2 describe the chosen OAE experiment locations and associated surface-ocean conditions that are expected to impact mCDR efficiency in these regions. The five experiments are representative of diverse dynamical and biogeochemical open-ocean conditions and include the following locations:

- *The North Atlantic Subduction (NAS)* experiment represents unique conditions found in subpolar regions associated with subduction driven by sea-ice formation and brine rejection, strong seasonally-driven vertical mixing, and seasonal biological CO_2 uptake.
- *The Western Boundary Current (WBC)* experiment is representative of mid-latitude conditions with strong horizontal currents and shear, along with intense vertical mixing.

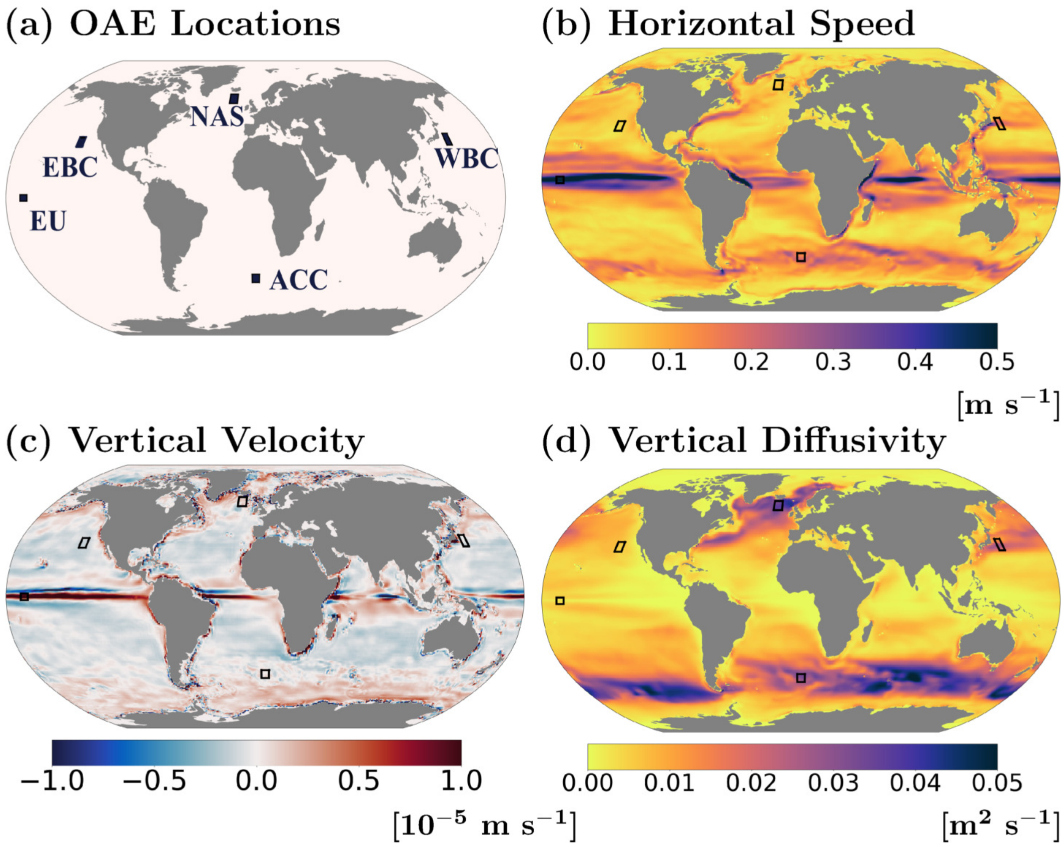

Figure 1. OAE experiments and time-mean values from January 1995 to December 2017 of ocean circulation fields from the baseline simulation. (a) Location of OAE experiments (black boxes show deployment sites), (b) magnitude of surface-ocean horizontal velocity, (c) mean vertical velocity over the upper-100 m, and (d) mean vertical diffusivity over the upper-100 m.

- *The Antarctic Circumpolar Current (ACC)* experiment represents conditions found in the Southern Ocean, which are associated with strong zonal currents, seasonal sea-ice cover, large-scale upwelling fronts, and seasonal biological uptake.
- *The Equatorial Upwelling (EU)* experiment is centered over the narrow upwelling zone of the Tropical Pacific Ocean and is characterized by strong CO_2 outgassing and seasonal biological uptake; its interannual variability tends to be dominated by El Niño–Southern Oscillation events (ENSO).
- *The Eastern Boundary Current (EBC)* experiment is centered over a region dominated by relatively-slow surface-ocean currents, coastal upwelling, and weaker primary production.

Experiment Name	Abbreviation	Spatial Bounds	Inject/Impact Area $\times 10^3$ km^2	Experiment Type	Potential Carbon Removed	$mCDR_{pot}$: Mean/Range mol C/mol Alk
North Atlantic	NAS	16°W–23°W	270	continuous	10^{-2} PgC yr^{-1}	0.854
Subduction		56°N–62°N	7,734	monthly-pulse	10^{-2} PgC	0.834–0.876
				yearly-pulse	12×10^{-2} PgC	
Western Boundary	WBC	144°E–148°E	267	continuous	10^{-2} PgC yr^{-1}	0.807
Current		31°N–38°N	14,155			0.792–0.826
Antarctic Circumpolar	ACC	3°E–3°W	268	continuous	10^{-2} PgC yr^{-1}	0.876
Current		45°S–50°S	13,033	monthly-pulse	10^{-2} PgC	0.866–0.899
				yearly-pulse	12×10^{-2} PgC	
Equatorial Upwelling	EU	165°W–170°W	267	continuous	10^{-2} PgC yr^{-1}	0.799
		2°S–2°N	38,353			0.783–0.811
Eastern Boundary	EBC	130°W–135°W	266	continuous	10^{-2} PgC yr^{-1}	0.834
Current		30°N–35°N	7,811			0.822–0.844

Table 2. List of OAE experiments: experiment names and their abbreviations used in this work; regional bounds of OAE deployment site; surface area of deployment site (deployment area) and OAE-impacted area (impact area) for continuous experiments characterized as an area where OAE-attributed CO_2 flux exceeds 0.1 mol C m^2 by the end of simulation; experiment type with respect to OAE duration; potential of removed CO_2 assuming typical ocean conditions; and mean $mCDR_{pot}$ over the deployment site from ECCO-Darwin (time-mean value over the simulation period and minimum and maximum monthly values, see Section 3.1 and Table 1 for definition of $mCDR_{pot}$). OAE deployment site locations are shown in Figure 1.

2.3 Rapid-mCDR: One-Dimensional Model for mCDR Simulation

At present time, the ECCO-Darwin simulations discussed in the previous section might be computationally too expensive for simulating and quantifying $mCDR_{eff}$ and therefore OAE additionality especially if a large number of OAE deployment sites and seasons are considered. Operational needs for quantification of real-world OAE might also require a more rapidly-deployable modeling framework.

For these reasons, and as an alternative numerically-efficient approach, we develop a one-dimensional model *rapid-mCDR* consisting of the following three equations:

$$\frac{\partial}{\partial t}\Delta\widehat{Alk} = -\frac{\partial}{\partial z}\overline{w}^{*}\Delta\widehat{Alk} + \frac{\partial}{\partial z}(\overline{K}^{*}\frac{\partial}{\partial z}\Delta\widehat{Alk}) + \frac{\delta_{z_k,0}}{\Delta z_1}f_{Alk}, \tag{4}$$

$$\frac{\partial}{\partial t}\Delta\widehat{DIC} = -\frac{\partial}{\partial z}\left(\overline{w}^{*}\Delta\widehat{DIC}\right) + \frac{\partial}{\partial z}(\overline{K}^{*}\frac{\partial}{\partial z}\Delta\widehat{DIC}) - \frac{\delta_{z_k,0}}{\Delta z_1}\Delta f_{CO_2}, \text{and} \tag{5}$$

$$\Delta f_{CO_2} = \overline{\kappa}^{*}(1-\overline{a}^{*}_{ice})\left(\overline{\frac{\partial pCO_2}{\partial Alk}}^{*}\Delta\widehat{Alk} + \overline{\frac{\partial pCO_2}{\partial DIC}}^{*}\Delta\widehat{DIC}\right), \tag{6}$$

where variables w and K are 3-D vertical velocity and diffusivity, κ is the surface-ocean piston velocity, and a_{ice} is sea-ice cover. The $\widehat{\varphi}$ and $\overline{\varphi}^{*}$ represent horizontally-integrated values of φ over the global ocean and horizontal-mean values of rapid-mCDR forcing φ over the OAE-impacted area, respectively. The value of $\delta_{z_k,0}$ is 1 for the uppermost rapid-mCDR vertical level and zero otherwise, and Δz_1 represents the ocean depth represented by that layer.

Equations 4 and 5 relate the time derivative of $\Delta\widehat{Alk}$ and $\Delta\widehat{DIC}$ (terms on the left hand side of these two equations) to its vertical advection and diffusion terms (first and second term on the right hand side of these equations) and prescribed Alk deployment rate or OAE-attributed CO_2 uptake (the last terms in Equations 4 and 5, respectively). These two equations are derived by simplifying budget equations (Supporting Information Equations 14 and 15), guided by analysis of these budget terms for the five representative OAE experiments (Supporting Information Text S4). The following two approximations are used: 1) the biological source term was neglected and 2) we linearized the products of vertical velocity and Alk perturbations as: $w\widehat{\Delta Alk} \approx \overline{w}^{*}\Delta\widehat{Alk}$ — this approximation neglects correlation between the vertical velocity and ΔAlk over the OAE-impacted regions. A similar approximation is made for DIC and diffusion terms in the conservation equation.

Equation 6 represents the horizontally-integrated net CO_2 flux due to OAE (i.e. OAE additionality) which is a function of ocean-surface perturbations $\Delta\widehat{Alk}$ and $\Delta\widehat{DIC}$.

The rapid-mCDR equations are solved for 50 vertical levels (that coincide with the ECCO-Darwin vertical levels) using a 1-day time step. The numerical finite difference scheme uses an implicit Euler method for time derivatives, which ensures numerical stability. A simple numerical stability analysis and sensitivity study indicates that the daily time step is sufficient (not shown). We assume that within the simulation time Alk and DIC perturbations will not reach the lowest model level and therefore bottom-level $\Delta\widehat{DIC}$ and $\Delta\widehat{Alk}$ is set to zero throughout the simulation. We initialize rapid-mCDR at January 1, 1995 (before the start of OAE deployments), at which time the Alk and DIC perturbations are set to zero. The model is then integrated through the ECCO-Darwin period (January 1st, 1995 to December 31st, 2017).

We note that there is some level of uncertainty in the method for horizontally averaging the required inputs to rapid-mCDR (i.e. for computation of $\overline{w}^*$, $\overline{K}^*$, and partial derivatives of $p\mathrm{CO_2}$ in Equation 6). To address this uncertainty, we use two different horizontal-averaging methods and quantify how they impact simulated $mCDR_{eff}$:

- *Deploy*: is the simplest approach where ocean conditions are horizontal means over the deployment site. This approach neglects the horizontal advection of OAE-impacted waters as they are transported away from the deployment site and into remote locations. Therefore, we expect the Deploy approach to be appropriate for OAE deployment sites that are associated with relatively weak horizontal advection or homogeneous ocean regions. Rapid-mCDR results obtained with this averaging method are referred as rapid-mCDR (Deploy).
- *HorAdv*: Improving on the Deploy approach, we also consider horizontal advection of OAE-impacted waters in a simplified manner. Ocean conditions are computed as weighted means over the region where OAE modifies surface $p\mathrm{CO_2}$; here the weights are proportional to the $p\mathrm{CO_2}$ perturbation Δp_{CO_2}. We expect this approach to capture the impact of horizontal transport on Alk and DIC cycling and CO_2 uptake, which the Deploy approach neglects. However, the HorAdv approach assumes that surface-ocean perturbations are indicative of horizontal transport

through the entire water column. The results of rapid-mCDR using this method are termed rapid-mCDR (HorAdv).

3 Results: ECCO-Darwin OAE Potential and Dynamical Efficiency

3.1 OAE Potential

As described in Section 2.1.1 and Supporting Information Text S3, surface-ocean $mCDR_{pot}$ is estimated diagnostically using *PyCO2SYS* from monthly-mean fields from 1) the baseline ECCO-Darwin simulation and 2) OceanSODA-ETHZ dataset (Gregor & Gruber, 2021), both covering the same time period from January 1995 to December 2017. The comparison of $mCDR_{pot}$ from the two datasets provides a qualitative measure of its uncertainty. Figure 2 shows time-mean $mCDR_{pot}$ for the global ocean and its climatological seasonal cycle from both datasets; Table 2 lists the ECCO-Darwin values for the 5 OAE deployment sites.

Time-mean $mCDR_{pot}$ reveals a pronounced meridional gradient, with the lowest values (approximately 0.75 mol C/mol Alk located in the tropics, progressively increasing poleward and eventually exceeding 0.9 mol C/mol Alk). For the same latitudinal range, values in regions dominated by western boundary currents tend to be lower than eastern boundary currents, exhibiting an anti-correlation with SST (Supporting Information Figure S1). This structure is consistent with the expected increase in CO_2 solubility at lower SST. Time-mean $mCDR_{pot}$ computed from both datasets exhibits similar features, with model-data differences generally not exceeding 0.025 mol C/mol Alk. One notable distinction is that OceanSODA-ETHZ values are marginally lower in eastern subtropical basins.

The climatological seasonal cycle of $mCDR_{pot}$ remains modest, not surpassing 0.05 mol C/mol Alk in either ECCO-Darwin or OceanSODA-ETHZ (Figure 2b). The most pronounced seasonal cycle occurs in northern mid-latitudes and polar regions. Peak values are found in western boundary currents regions and are likely associated with elevated seasonality in SST (Jo et al., 2022). Although both ECCO-Darwin and OceanSODA-ETHZ exhibit similar seasonal patterns of $mCDR_{pot}$, the values from OceanSODA-ETHZ tend to have larger magnitudes. Across the five deployment sites, mean $mCDR_{pot}$ ranges from 0.799 mol C/mol Alk (EU) to 0.854 mol C/mol Alk (NAS), while climatological seasonal cycle values do not exceed 0.05 mol C/mol Alk (Table 2). In summary, these

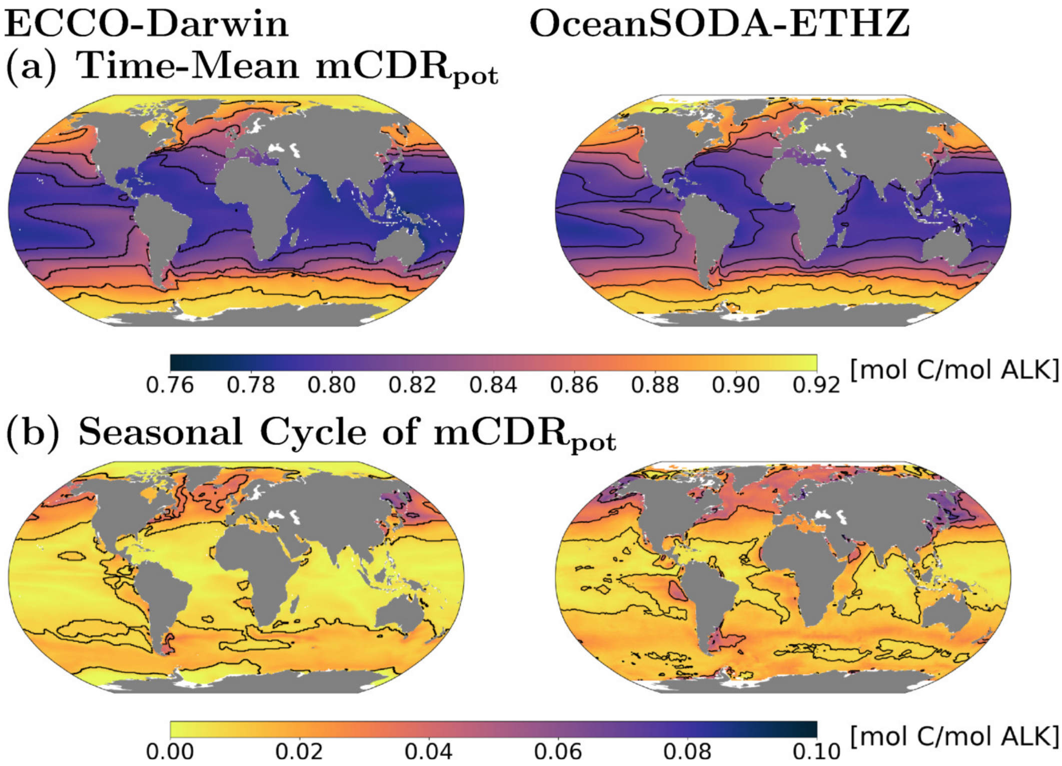

Figure 2. $mCDR_{pot}$ from the baseline ECCO-Darwin simulation (left) and OceanSODA-ETHZ dataset (right) showing (a) time-mean values over the ECCO-Darwin period (January 1995 to December 2017) and (b) magnitude of climatological seasonal cycle.

findings suggest that, in the current climate, $mCDR_{pot}$ is adequately represented by time-mean values, except in localized regions that experience pronounced seasonality. Both ECCO-Darwin and OceanSODA-ETHZ demonstrate similar spatial structure; hence in the subsequent section we use only ECCO-Darwin .

In summary, as depicted in Figure 2, the most effective OAE deployments, solely from a CO_2 solubility perspective, would be over polar oceans — regions characterized by the highest potential for CO_2 removal. However, in the next sections, when we consider ocean sea-ice and dynamical effects that are captured by the mCDR efficiency factor, this narrative will substantially change.

3.2 OAE Impact on Ocean State for Continuous OAE experiments

Before quantifying OAE efficiency, we first investigate the impact of OAE on the ocean state for the five continuous experiments. Because of the larger Alk perturbation, our continuous experiments serve as a upper limit of ocean state perturbations. These results serve as an illustration of expected OAE impacts, because the environmental impacts are expected to scale with the magnitude of injected Alk. We examine the spatial patterns of atmospheric CO_2 uptake and alteration of surface-ocean pH. We also characterize the vertical transport of OAE-impacted waters.

For the five continuous OAE experiments, Figure 3 shows a map of time integrated net CO_2 flux due to OAE from the atmosphere into the ocean by the end of the ECCO-Darwin simulation. The OAE additionality by the end of simulation can be obtained by integrating these values over the surface ocean. For all OAE deployments, integrated net CO_2 flux is largest close to the deployment site and its footprint is indicative of near-surface horizontal advection, with the following key features:

- For NAS, the North Atlantic and the Norwegian Currents transport OAE-modified waters towards high-latitude regions, with the flow bifurcating near Iceland. As a result, the largest values of net CO_2 flux are found at, or north of the deployment site.
- For WBC and ACC, predominant zonal transport result in the largest net CO_2 flux values located primarily east of the deployment site. In particular, the strong Antarctic Circumpolar Current in ACC spreads net CO_2 flux eastward over a large region of the Southern Ocean.

- For EU, equatorial upwelling and upper-ocean zonal flow both north and south of the equator spreads the net CO_2 flux footprint over most of the tropical/subtropical Pacific Ocean. The signature of cumulative net CO_2 flux for EU covers the largest horizontal area (see Table 2), while the maximum magnitude is the lowest of all 5 experiments.
- For EBC, the anticyclonic circulation associated with the subtropical gyre advects OAE-impacted waters towards the southwest, spreading the net CO_2 flux footprint west of Southern California and Baja Mexico.

One important concern regarding OAE is modification of ocean pH, which might inadvertently harm marine ecosystem health (e.g., Bach et al., 2019). Figure 4 shows the maximum pH modification due to OAE for all five continuous experiments. These spatial patterns are approximately correlated with spatial patterns of high net CO_2 flux. We note that none of the continuous experiments change OAE-attributed pH more than 0.05 with respect to the background state, which is far less than what was considered a safe limit in He and Tyka (2023).

To illustrate the depth and temporal change in the disequilibrium of OAE-impacted waters across the five continious OAE experiments, Figure 5a shows the temporal evolution of the depth above which 95% of the deployed Alk remains. We adopt this depth threshold as a metric to demarcate OAE-modified waters from those unaffected by OAE. Figure 5b shows time series of the horizontally-averaged equilibration coefficient $mCDR_{equil}$ for each of the experiments (mean over upper 100 m shown) and Figure 5c shows the spatial distribution of $mCDR_{equil}$ at the end of the simulation. $mCDR_{equil}$(described in detail in Supporting Information Text S4, Section 3), is similar to $mCDR_{eff}$ but is a local value computed for a particular volume of seawater in ECCO-Darwin.

For all OAE experiments, the OAE perturbation spreads to deeper waters with elapsed time after deployment, with large differences occurring in the depth of the OAE impact across all experiments. By the end of the simulation, the Alk perturbation reaches the depth in excess of 2000 m for NAS and roughly 1000 m for ACC. For the other three experiments, Alk perturbations remains much closer to the ocean surface and the ocean waters below 500 m remain largely unaffected.

The time evolution of $mCDR_{equil}$ for all experiments exhibits an approximately exponential increase, overlaid by strong seasonality (Figure 5b). The exponential increase

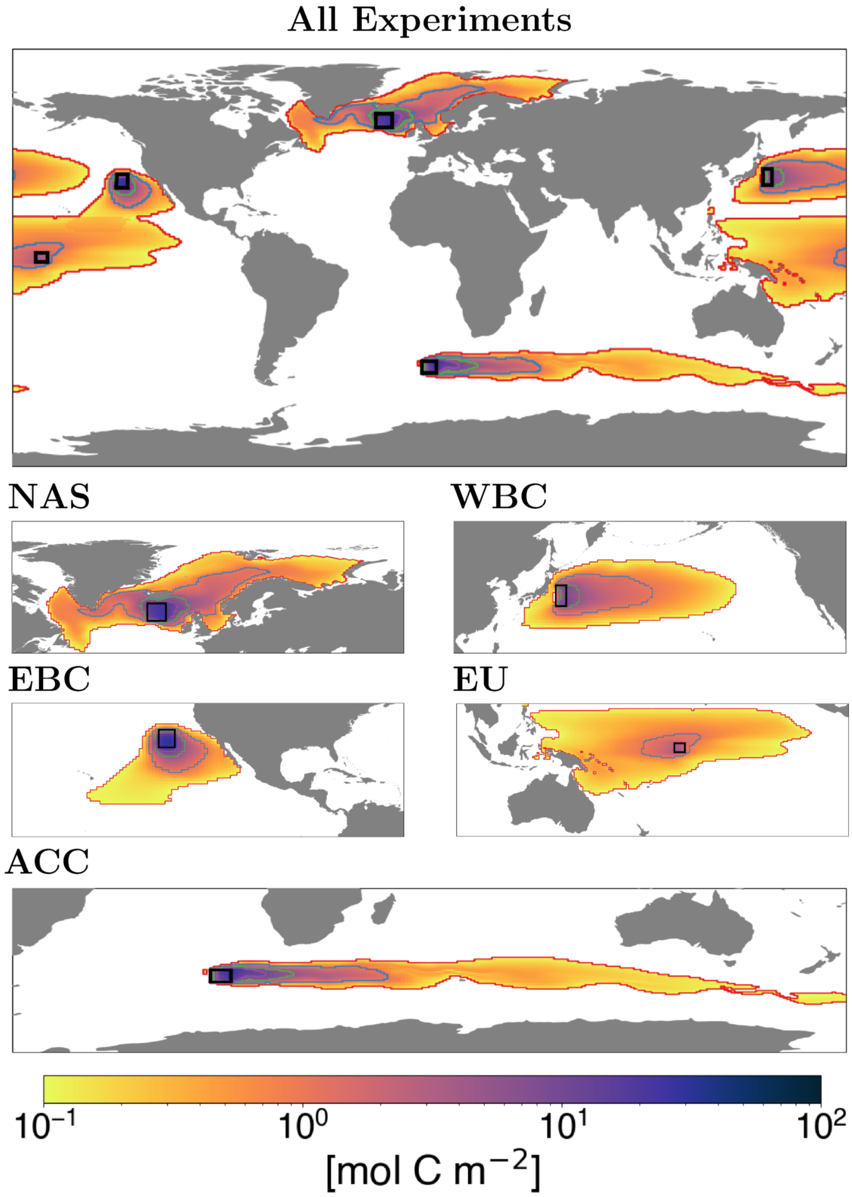

Figure 3. Time-integrated net CO_2 flux due to OAE from January 1995 to December 2017 for the 5 continuous OAE experiments. The color scale is logarithmic, highlighting variations in CO_2 uptake intensity and isolines represent DIC increases of 0.1, 1, 5, 10, and 50 mol C m^{-2}. Black boxes show OAE deployment sites. Upper panel shows all 5 OAE experiments across the global ocean; lower panels show individual OAE experiments.

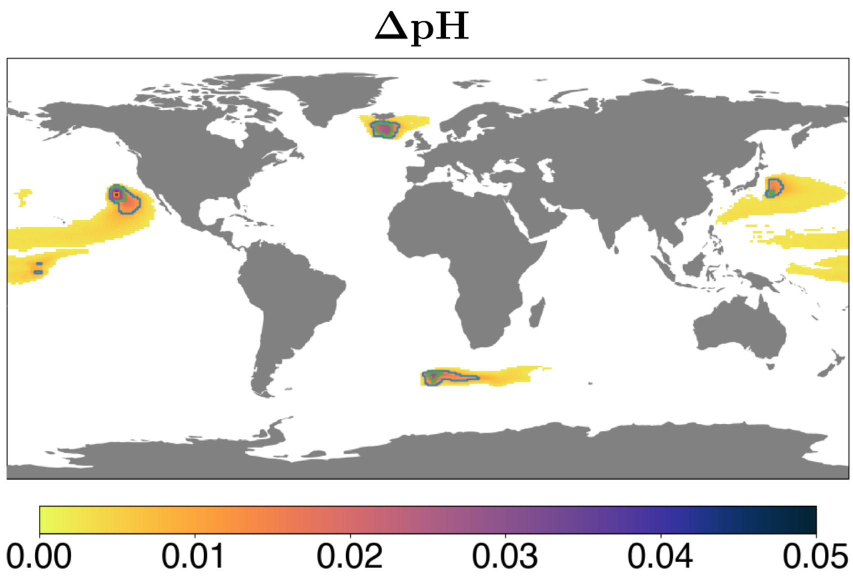

Figure 4. Maximum pH perturbation across time and depth (maximum ΔpH) due to OAE for the 5 continuous experiments. Only values above 0.0025 are shown. Isolines represent maximum ΔpH values of 0.01, 0.02, 0.03, and 0.04.

is associated with the long time scale of CO_2 reequilibration and the overlaid seasonality is associated with the strong seasonality of the mixed layer depth (MLD) and associated transport of Alk-modified water below the MLD as the MLD shoals (detrainment), and its re-entrainment as the MLD deepens.

$mCDR_{equil}$ tends to be highest for ACC and is associated with the shortest reequilibration time scale, despite the fact that the deployed Alk mixes relatively deep at this site (Figure 5b). The short reequilibration time scale is consistent with the high CO_2 piston velocity over this region, associated with strong zonal winds (e.g., Jones et al., 2014). The seasonality of $mCDR_{equil}$ is strongest at NAS and WBC; in particular, the former is consistent with strong seasonality in MLD and vertical transport of OAE-attributed Alk and DIC (Supporting Information Figures S3 and S4). Figure 5c shows that the lowest values of $mCDR_{equil}$ are found 1) close to the deployment sites where ocean-atmosphere CO_2 reequilibration has not been fully realized and 2) increases as OAE-impacted waters spread into remote locations.

In Supporting Information Text S5, we discuss horizontally-integrated budgets for DIC and Alk perturbations for the continuous OAE experiments. These budgets separate and quantify the contributions of key processes that modify DIC and Alk pertur-

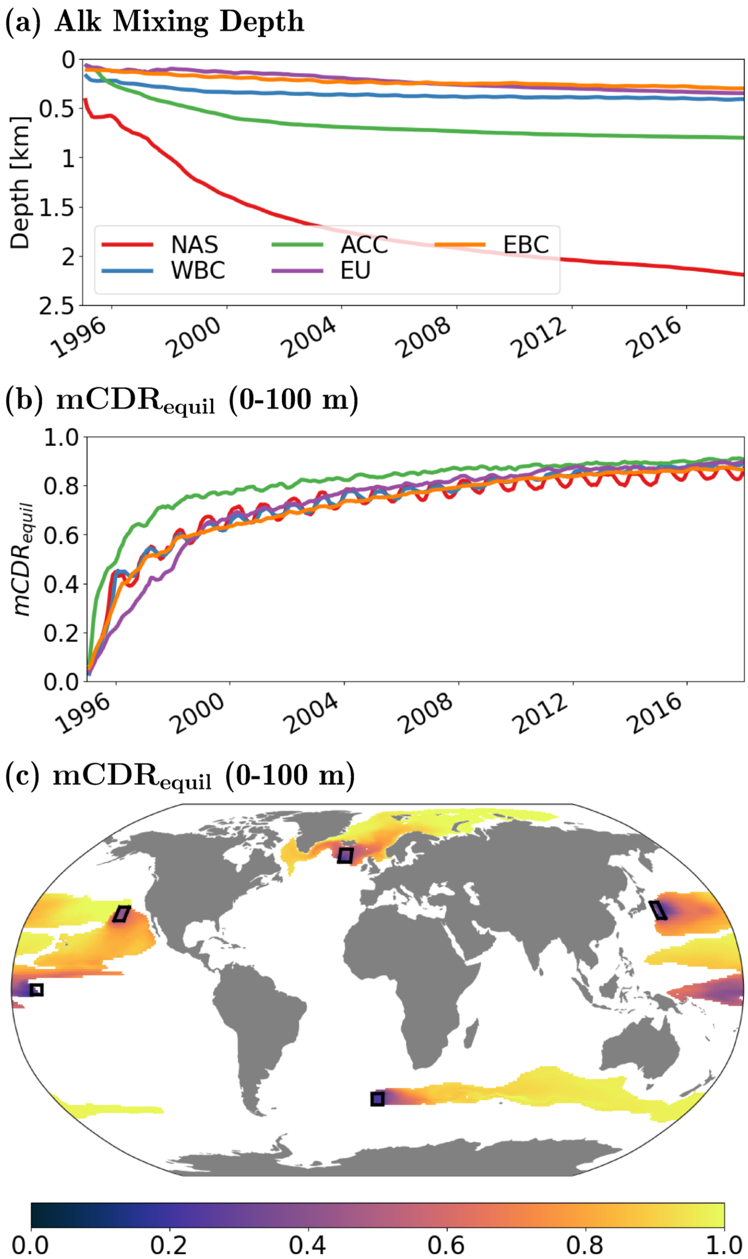

Figure 5. Continuous OAE experiments: (a) time series of the depth that separates OAE-impacted waters from unmodified waters, (b) time series of $mCDR_{equil}$ in the upper ocean (mean value over the upper 100 m), and (c) spatial pattern of $mCDR_{equil}$ in the upper ocean (mean value over the upper 100 m) at the end of the simulation.

bations. With the exception of the air-sea interface, where the DIC and Alk perturbations increase due to additional CO_2 flux from the atmosphere and the prescribed OAE Alk flux, respectively, changes to DIC and Alk perturbations are predominantly dominated by vertical ocean dynamics.

Across all deployment sites, excluding EU, a pronounced seasonality characterizes the strength of vertical mixing and advection, coinciding with variations in MLD. As the MLD deepens, DIC and Alk perturbations are transported into deeper waters, potentially sequestering them from the atmosphere (which inhibits or delays OAE additionality) until the MLD shoals again. Notably, the relative influence of vertical advection and mixing varies significantly by deployment site. The depth of the MLD and its seasonal variability differs substantially among sites, with NAS having the deepest seasonal MLD.

3.3 Efficiency of Alk Enhancement

3.3.1 Continuous OAE Experiments

For the five continuous OAE experiments, Figure 6 shows three key aspects of mCDR efficiency $mCDR_{eff}^{cont}$. In panel (a), we show time-mean $mCDR_{eff}^{cont}$ from the start of the OAE deployment (i.e., January 1, 1995) to the time shown on the x-axis. These curves represent the fraction of OAE potential realized by the time indicated on the x-axis; we refer to this quantity as *realized mCDR potential*. The realized mCDR potential is thus an important metric for quantifying the OAE additionality of continuous deployments.

Figure 6b shows $mCDR_{eff}^{cont}$ filtered with a centered 1-year running mean. These curves relate instantaneous Alk deployment to instantaneous CO_2 uptake, expressed using efficiency terms and with seasonal cycle removed. This is because $mCDR_{eff}^{cont}$ and CO_2 uptake are basically proportional to each other (Equation 3). For deployments associated with weak interannual variability in $mCDR_{eff}^{cont}$, we expect that these curves also closely represent the mean efficiency of pulse deployments over a seasonal cycle. Figure 6c shows the seasonal cycle of $mCDR_{eff}^{cont}$ over the last ten years of simulation. The deployment locations associated with significant seasonal cycle indicate significant seasonality of CO_2 uptake. For instantaneous OAE deployments, this is likely related to mCDR efficiency being dependent on deployment season, which we further investigate in Section 3.3.2.

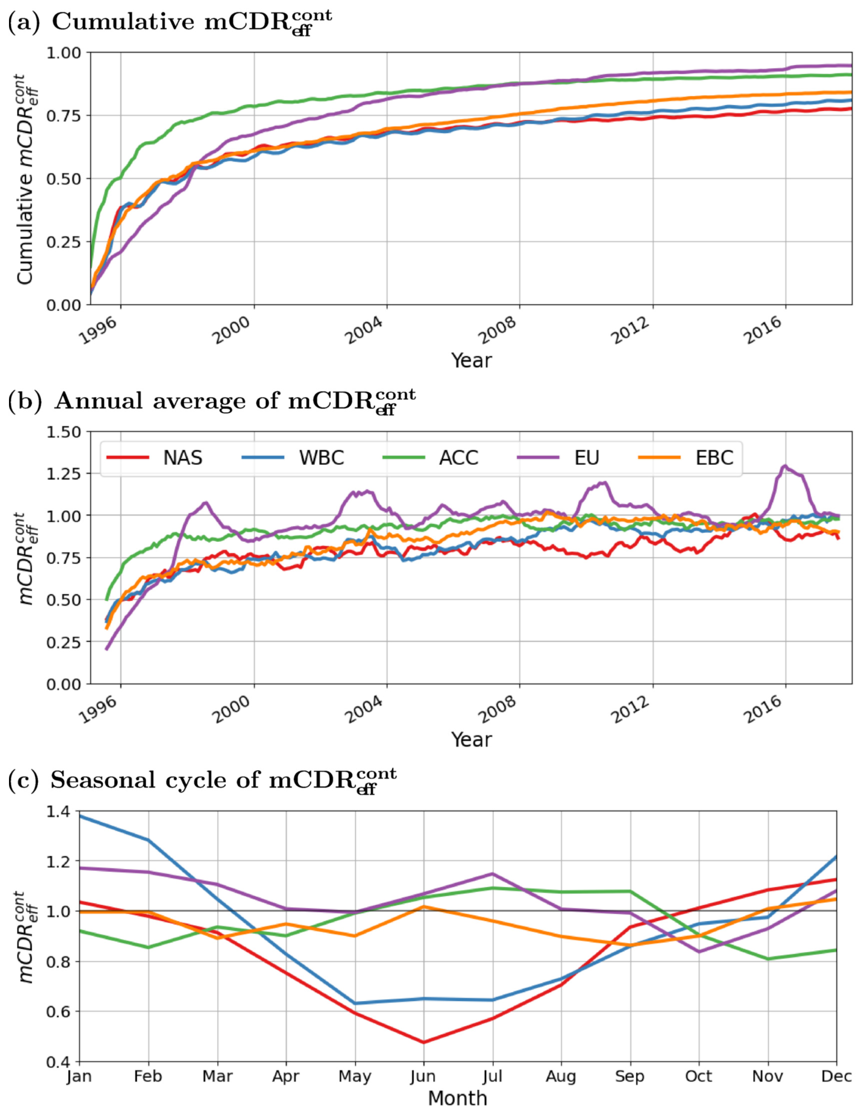

Figure 6. Three different key aspects of $mCDR_{eff}^{cont}$ efficiency: (a) time-mean values from the start of the OAE deployment to time indicated on the x-axis; (b) centered 1-year running-mean values; and (c) seasonal cycle over the last simulation decade calculated as monthly-mean values over the last 10 years of simulation. The colors represent the five different OAE deployments, as indicated by the legend.

For all continuous experiments, the realized mCDR potential curves increase in an approximately exponential manner with time after start of deployment (Fig. 6a), with the following key characteristics:

- ACC is associated with the most rapid increase of realized mCDR potential, where values exceed 0.75 within 5 years after the start of OAE and also reach one of the highest values by the end of the simulation (0.91). This is consistent with the most rapid increase of $mCDR_{equil}$ in the upper ocean as shown in Figure 5.
- For all deployments, EU is associated with the slowest initial increase of realized potential, consistent with the slowest increase of $mCDR_{equil}$. However, after roughly 13 years after deployment its values reach that of the ACC and by the end of the simulation, EU reaches the highest value of all simulations, 0.95. The realized mCDR potential for this location diverges from the exponential shape due to strong interannual variability of $mCDR_{eff}^{cont}$, which we discuss below.
- For the other three experiments (EBC, WBC, and NAS), the realized mCDR potential behaves remarkably similar over the first decade after the start of deployments and by the end of 2017 their values differ by only a few percent each (0.84, 0.81, and 0.77 for EBC, WBC, and NAS, respectively).

Figure 6b shows similar exponential behavior of $mCDR_{eff}^{cont}$ as discussed for the realized mCDR potential above, but it also reveals interannual variability in $mCDR_{eff}^{cont}$. Note that for most of the experiments, $mCDR_{eff}^{cont}$ is also associated with a strong seasonal cycle which is filtered from the plots shown on Figure 6b. EU is associated with the largest interannual variability of $mCDR_{eff}^{cont}$, superimposed on its exponential and subsequent tapered increase. This interannual variability is positively correlated with the multivariate El-Niño/Southern Oscillation (ENSO) index (Wolter & Timlin, 2011) (not shown), demonstrating that ENSO has a substantial impact on mCDR efficiency in the Tropical Pacific Ocean. We note that other locations also exhibit interannual variability in $mCDR_{eff}^{cont}$, although it is lower than EU. The values of running mean $mCDR_{eff}^{cont}$ can exceed one for a limited time period, which is most evident for the EU experiment. This does not mean that OAE efficiency exceeds 100%, as the overall efficiency is related to the time-mean $mCDR_{eff}^{cont}$ values in Figure 6a and which do not exceed the value of one.

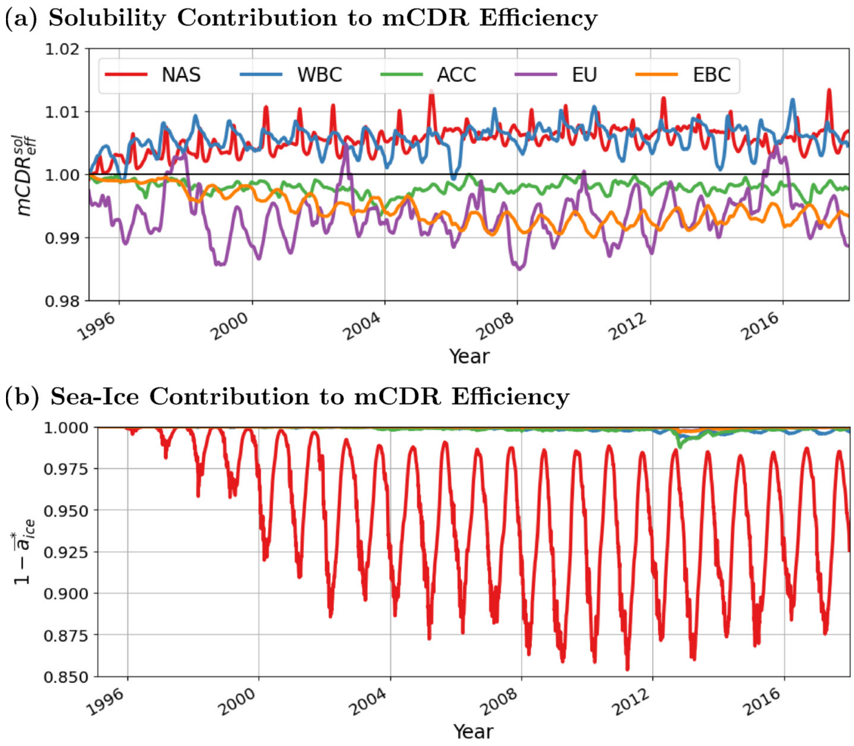

Figure 7. Impact of CO_2 solubility and sea-ice cover on $mCDR^{cont}_{eff}$. The five colors represent the different OAE experiments, as shown in the legend.

Figure 6c shows that $mCDR^{cont}_{eff}$ for NAS and WBC are associated with strong seasonality, yielding maximum values (and thus strongest ocean CO_2 uptake) in winter and minimum values in summer. Peak monthly values are up to 40% lower/higher compared to annual-mean values. In ACC, the magnitude of the seasonal cycle of $mCDR^{cont}_{eff}$ is roughly half that of NAS and is shifted in phase roughly 6 months due to its location in the southern hemisphere. We emphasize that the seasonal cycle of $mCDR^{cont}_{eff}$ is not directly related to the seasonal cycle of mCDR efficiency for the pulsed experiments. We discuss the relations between the two seasonal cycles in the next section.

Next we discuss the impact of one of the key simplifications when estimating $mCDR^{cont}_{eff}$. As described in Section 2.1.2, we defined $mCDR^{cont}_{eff}$ with respect to $mCDR_{pot}$ at the deployment site and time (Equation 3); however, its values at all locations and times of OAE-driven air-sea CO_2 exchange should be used. Figure 7a shows $mCDR^{sol}_{eff}$, which represents the multiplicative factor with which the $mCDR^{cont}_{eff}$ should be corrected to account for this simplification (Supporting Information Text S4). $mCDR^{sol}_{eff}$ values greater/smaller than one represent fractional increase/decrease of $mCDR^{cont}_{eff}$ due to a change in $mCDR_{pot}$

as the perturbation spreads from the deployment site to remote locations. This primarily results from changes in CO_2 solubility due to cooling or warming of OAE-impacted waters.

Figure 7a shows that the impact of the above-discussed simplification is small and does not modify $mCDR_{eff}^{cont}$ by more than 2% and rarely more than 1% for any of the experiments. In NAS and WBC, northward and eastward flows, respectively, transport Alk-enhanced waters to regions with lower SSTs and higher $mCDR_{pot}$, therefore the $mCDR_{eff}^{sol}$ exceeds values of one. For the other three locations, horizontal transport results in a decrease of $mCDR_{eff}^{cont}$. In summary, we show that using the deployment site value of $mCDR_{pot}$ is appropriate for the experiments described here. Figure 7b shows the impact of sea-ice on $mCDR_{eff}^{cont}$, as sea-ice cover inhibits air-sea CO_2 exchange and limits mCDR efficiency. The impact of sea-ice cover is substantial only in NAS during winter, as Alk-impacted waters are transported polarwards into seasonally ice-covered regions.

3.3.2 Pulse OAE Experiments

As described in Section 2.2.4, we use three targeted pulse OAE experiments for the NAS and ACC deployments. Each uses a different OAE deployment strategy, Yr1995, Jan1995, and Jul1995, to further understand how $mCDR_{eff}$ depends on the season of deployment. Figure 8 shows time series of $mCDR_{eff}$ and $mCDR_{exch}$ (which is essentially a normalized net CO_2 flux and is defined in Supporting Information Text S2).

For the three NAS experiments (Figure 8a), the time evolution of $mCDR_{eff}$ is highly dependent on the month of Alk deployment. By the end of simulation, Alk deployed in summer (Jul1995) reaches an efficiency of roughly 0.9 while winter deployment (Jan1995) is only slightly above 0.6; the efficiency of the annual deployment (Yr1995) lies between these two extreme values. In addition to seasonally-dependent efficiency for NAS, all three experiments show strong seasonality in $mCDR_{exch}$, with the highest values occurring during spring; this coincides with the deepest MLD in the region surrounding NAS (see Supporting Information Figure S3).

For the NAS experiments, seasonality of $mCDR_{eff}^{cont}$ and $mCDR_{exch}$ (Figures 6c and 8a, respectively) are generally in phase, and track the seasonality of CO_2 flux. However, $mCDR_{eff}$ is not the highest for the deployment months associated with the highest CO_2 flux. Instead OAE deployment a few months prior to the maximum value of $mCDR_{exch}$

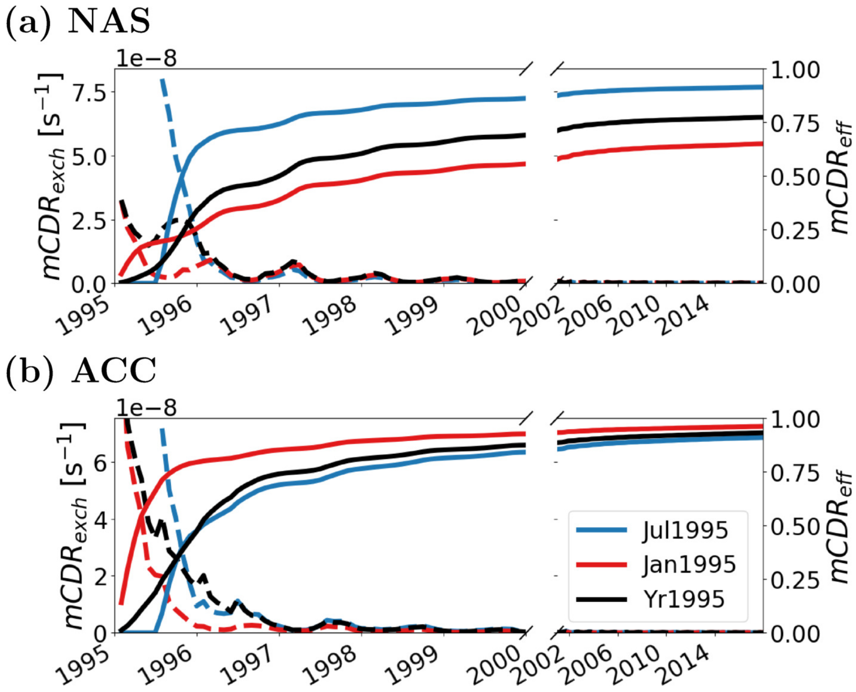

Figure 8. Monthly-pulse and yearly-pulse experiments for (a) NAS and (b) ACC. Dashed lines show $mCDR_{exch}$ (y-axis shown on left-hand-side of figure); solid lines show $mCDR_{eff}$ (y-axis shown on right-hand-side of figure).

is associated with the highest overall efficiency. In ACC, Jul1995 is associated with lower $mCDR_{eff}$ compared to Jan1995, which is consistent with results in NAS, considering that these two locations are located in different hemispheres. The difference between these two experiments is only a few percent at the beginning of 2017, which also indicates a weaker seasonal cycle of $mCDR_{eff}^{cont}$ and $mCDR_{exch}$.

4 Results: $mCDR_{eff}$ from Rapid-mCDR

In this section, we first compare rapid-mCDR against ECCO-Darwin and discuss the difference in results when using the two horizontal-averaging methods described in Section 2.3. Then as an example use case, we use rapid-mCDR to understand how and why mCDR efficiency varies latitudinally across a section in the central Pacific Ocean.

4.1 Evaluation of rapid-mCDR against ECCO-Darwin for the 5 OAE Deployments

Figure 9 shows a comparison of continuous mCDR efficiency, $mCDR_{eff}^{cont}$, from rapid-mCDR against ECCO-Darwin for all five continuous OAE experiments. While the main output from rapid-mCDR is the OAE additionality, we prefer to show $mCDR_{eff}^{cont}$ as it disentangles the effect of $mCDR_{pot}$. For each OAE experiment, both rapid-mCDR (Deploy) and rapid-mCDR (HorAdv) simulations are performed. The compared quantities on Figure 9 include:

1. Scatter plots of monthly-mean $mCDR_{eff}^{cont}$ between ECCO-Darwin and two rapid-mCDR versions. This provides a measure of the overall skill of rapid-mCDR in emulating CO_2 uptake efficiency (left panel).
2. Time series of $mCDR_{eff}^{cont}$ using a centered-running mean, showing possible bias in rapid-mCDR simulations (middle panel).
3. Seasonal cycle of $mCDR_{eff}^{cont}$, further indicating the skill of rapid-mCDR and possible seasonal bias (right panel).

In addition, Supporting Information Figure S5 shows the agreement of $mCDR_{equil}$ between the two rapid-mCDR versions and ECCO-Darwin. This comparison demonstrates in a compact form the agreement in vertical transport of both Alk and DIC between rapid-mCDR and ECCO-Darwin.

For NAS, Figure 9a shows that $mCDR_{eff}^{cont}$ from rapid-mCDR (HorAdv) agrees extremely well with ECCO-Darwin for the entire duration of the OAE deployment. The coefficient of determination for the monthly-mean values is $R^2 = 0.9$. The rapid-mCDR (HorAdv) slightly underestimates annual-mean values of $mCDR_{eff}^{cont}$ during the first part of the period, but this underestimation is less than 0.05. The seasonal cycle of $mCDR_{eff}^{cont}$ is extremely well simulated by this version of rapid-mCDR. As expected, rapid-mCDR (Deploy) does not agree as well with ECCO-Darwin and generally overestimates $mCDR_{eff}^{cont}$ during most of the simulation period, except for the first five years after start of the OAE deployment. While this overestimation is primarily due to winter period, as revealed by the comparison of the seasonal cycle, the overestimation remains present to some degree throughout the year. The winter overestimation is likely dominated by the absence of sea-ice for the rapid-mCDR (Deploy), which the ECCO-Darwin and rapid-mCDR (HorAdv) are impacted by. As discussed above, Figure 7b indicates that the spatial mean of sea-ice area taken over the deployment region can reach up to 0.15 in the winter period, which is expected to arrest winter CO_2 uptake (and therefore $mCDR_{eff}^{cont}$) by roughly that fraction.

For WBC (Figure 9b), both version of rapid-mCDR somewhat overestimate annual-mean $mCDR_{eff}^{cont}$, where as expected, rapid-mCDR (HorAdv) better represents ECCO-Darwin. This is the case for time series of annual-mean values, as well as the coefficients of determination which are 0.90 and 0.76 for rapid-mCDR (HorAdv) and rapid-mCDR (Deploy), respectively; the seasonal cycle from both versions of rapid-mCDR well reproduces ECCO-Darwin. For ACC (Figure 9c), both version of rapid-mCDR well reproduce all aspects of $mCDR_{eff}^{cont}$, with rapid-mCDR (HorAdv) preforming better than rapid-mCDR (Deploy). The difference from the two rapid-mCDR versions is small, despite the OAE perturbation extending over a large meridional distance (Figure 5).

For EU, the agreement of $mCDR_{eff}^{cont}$ between the two rapid-mCDR simulations and ECCO-Darwin is the poorest of all five OAE experiments, with a R^2 of 0.74 for rapid-mCDR (HorAdv) and only 0.03 for rapid-mCDR (Deploy). The annual-mean comparison shows that rapid-mCDR (Deploy) is unable to well represent multi-annual variability, which is strong in this deployment location. rapid-mCDR (HorAdv) represents this multi-annual variability better likely due to capturing horzontal advection.

In EBC, rapid-mCDR (Deploy) significantly underestimates $mCDR_{eff}^{cont}$, especially after approximately a decade after the start of Alk deployment, while rapid-mCDR (HorAdv) agrees somewhat better with ECCO-Darwin. The cause of this underestimation is likely similar as for the EU deployment, where after a number of years the OAE-impacted waters enter the tropical Pacific, which is strongly impacted by the ENSO variability.

In Figure 10 we show the ability of rapid-mCDR to represent mCDR efficiency for the three pulse experiments for NAS and ACC, which were shown to strongly vary with deployment season.

For NAS, rapid-mCDR agrees very well with ECCO-Darwin over the first five years after deployment and shows skill in representing seasonally-varying $mCDR_{eff}$ as discussed above. By the end of the simulation period, rapid-mCDR somewhat overestimates $mCDR_{eff}$; this overestimation is consistent for all three experiments. For ACC, $mCDR_{eff}$ is over-

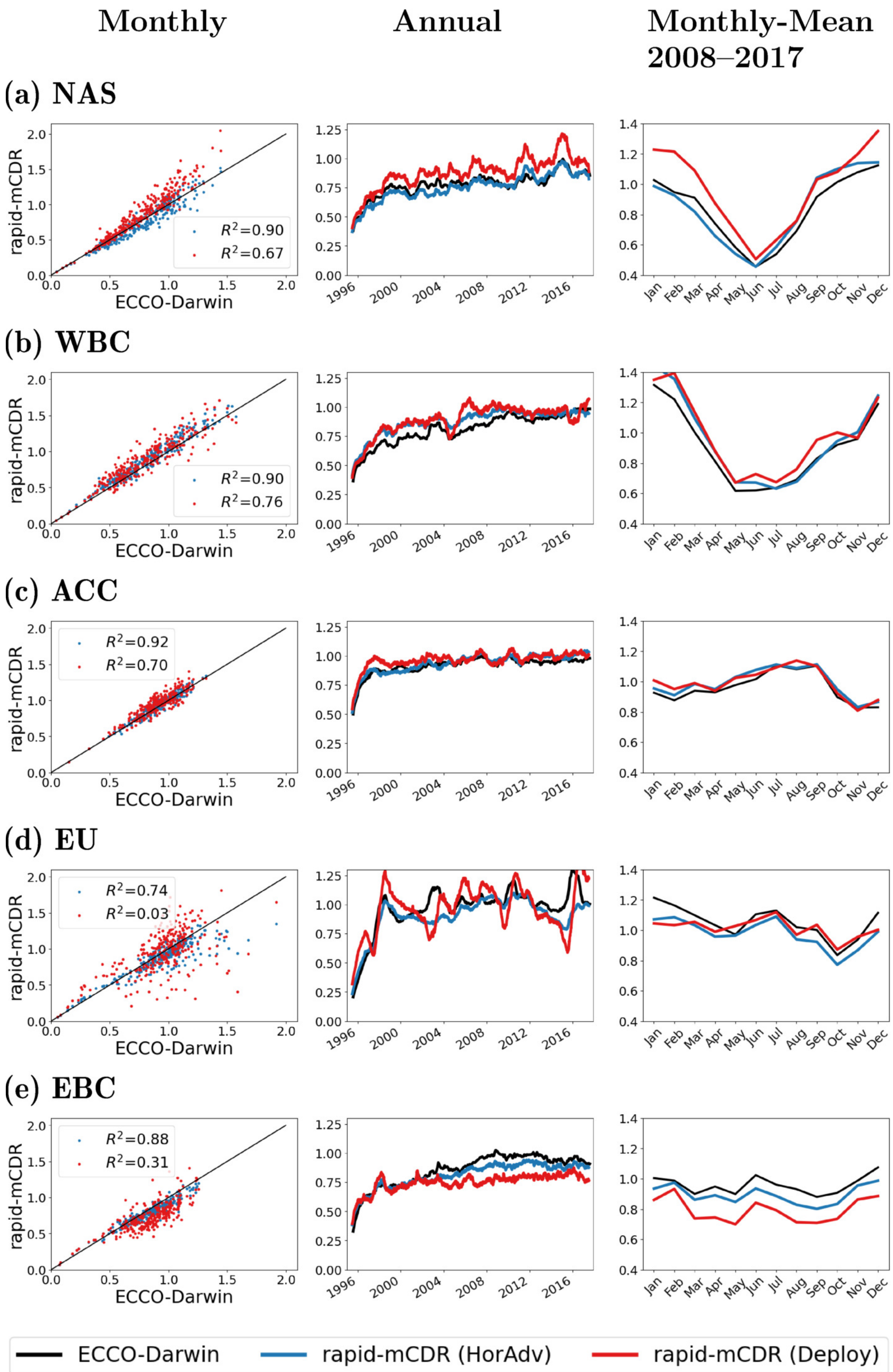

Figure 9. Continuous OAE experiments. Comparison of $mCDR_{eff}^{cont}$ from both versions of rapid-mCDR against ECCO-Darwin. Left panels (a–e) show monthly-mean rapid-mCDR vs. ECCO-Darwin and associated R^2 values. Middle panels show time series using a 12-month centered-running mean; right panels show monthly-mean values for a zoom in period during the last 10 years of simulation. Blue and red lines represent rapid-mCDR (HorAdv) and rapid-mCDR (Deploy), respectively. Black line in middle and right panels shows ECCO-Darwin results.

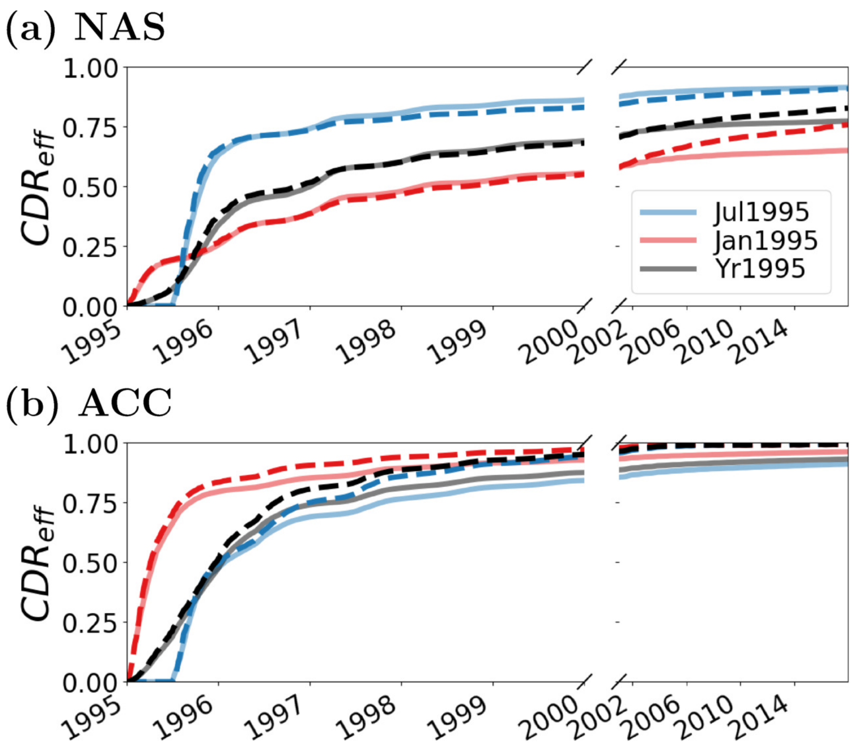

Figure 10. $mCDR_{eff}$ for monthly-pulse and yearly-pulse experiments in (a) NAS and (b) ACC. Solid lines show ECCO-Darwin, dashed lines show rapid-mCDR (HorAdv).

estimated by rapid-mCDR — a result that is consistent with the continuous OAE experiments in this region. Rapid-mCDR predicts that by the end of the simulation period $mCDR_{eff}$ approaches a value of one, which is roughly 0.1 larger than ECCO-Darwin.

4.2 Expanding Rapid-mCDR to Ocean-basin Scales

In this section, we provide an example use case of rapid-mCDR to characterize $mCDR_{eff}$ across spatial and temporal scales that might be prohibitively expensive to examine with ECCO-Darwin. We also use rapid-mCDR to identify physical processes that adversely impact $mCDR_{eff}$.

We simulate Alk deployment across the meridional extent of the Pacific Ocean, centered on 165°W. The deployment sites are spaced 1°apart in latitude from 77°S to 55°N. This latitudinal range is chosen so that deployment sites represent open-ocean conditions. Each site covers a rectangular area of 10° wide in longitude and 3° wide in latitude; the central deployment site locations are shown on Fig. 11a. For all of these sites, we use rapid-mCDR (Deploy) version of the model and where the inputs, which are taken from the baseline ECCO-Darwin simulation. At each deployment site, we performed three experiments using rapid-mCDR — these are equivalent to the three ECCO-Darwin pulse experiments discussed in Section 2.2.4: *Yr1995*, *Jul1995*, and *Yr1995*. As with ECCO-Darwin, these experiments are run until December 31, 2017 and the values of $mCDR_{eff}$ are evaluated at the end of simulation.

Furthermore, to isolate the role of physical processes (vertical advection, vertical diffusivity, and sea-ice cover) on $mCDR_{eff}$, we performed three additional sets of rapid-mCDR sensitivity experiments to separate and quantify the impact of each of these factors. These three sensitivity experiments are based on the Yr1995 experiment described above with the following modifications: 1) *Yr1995-w0* is an experiment with vertical velocity set to zero, 2) *Yr1995-k0* is an experiment with vertical diffusivity set to zero, and 3) *Yr1995-ice0* is an experiment with no sea-ice cover (i.e., open-water conditions).

Figure 11b shows $mCDR_{eff}$ for the Yr1995 experiment at the end of the simulation, plotted against central latitude of deployment site, along with profiles of time-mean vertical velocity and vertical diffusivity. Figure 11c shows profiles of normalized Alk perturbation (i.e., $\Delta\widehat{Alk}$ normalized by the maximum value of all experiments) at the end of simulation time to show the vertical extent of the OAE perturbation.

We find that $mCDR_{eff}$ is strongly dependent on deployment site location, with the largest values found in tropical regions, mid-latitude and polar regions in the southern hemisphere (between approximately 60–50°S) and mid-latitudes in the northern hemisphere (between approximately 40–50°N). The lowest values (less than 0.5) are generally found in subtropical regions and in the northern extent of polar regions. Except for polar regions in the southern hemisphere, high $mCDR_{eff}$ values are found at locations associated with significant ocean upwelling and outcropping and the lowest values are located in downwelling regions. Figure 11c shows that high values of $mCDR_{eff}$ are associated with Alk perturbations that remain close to the surface; for locations associated with low values, Alk perturbations are either transported to depth or spread over a substantial vertical extent.

Figure 12 shows $mCDR_{eff}$ for the three deployment seasons (Figure 12a) and for the three sensitivity experiments (Figure 12b); these quantities are compared against the Yr1995 experiment (Figure 12a,b, black lines) and CDRpot and sea-ice cover (Figure 12c).

All quantities are plotted as a function of deployment site latitude. For locations in mid-latitudes and subtropical regions, there is strong dependence of $mCDR_{eff}$ on the deployment season. Summer months are generally associated with higher efficiency compared to winter, which is consistent with the pulse experiments results for NAS and ACC (see Section 3.3). The difference of $mCDR_{eff}$ between the deployments in summer season reach up to 0.3 higher values than the deployments in the winter season.

The experiments shown in Figure 12b demonstrate that for polar OAE deployment sites in the southern hemisphere, which are under the influence of seasonal sea ice, the ice cover efficiently prevents CO_2 uptake and therefore these regions are associated with low values of $mCDR_{eff}$. Removing sea-ice cover in rapid-mCDR (Figure 12b, orange line) increases $mCDR_{eff}$ to values close to one below roughly 50°S. Therefore, our simulations suggest that mCDR efforts will be much less effective in this, and other ice-covered regions.

From the two dominant ocean circulation processes, vertical velocity and diffusivity, we find that vertical velocity dominates low-efficiency regions (i.e., the role of vertical diffusivity here is second order). There is only a small increase of $mCDR_{eff}$ with respect to the Yr1995 experiment if the vertical diffusivity is set to zero (Figure 12b, purple line). However, if the vertical velocity is set to zero $mCDR_{eff}$ becomes close to one for most of the deployment sites (Figure 12b, green line), except for ice-covered regions in the southern hemisphere. Figure 12c shows $mCDR_{pot}$ vs. latitude; the lowest values are found in the tropical/subtropical regions of the Pacific Ocean, with increasing values towards the poles. The variability of $mCDR_{pot}$ over each deployment site is small (Figure 12c, gray shaded envelope) compared to the latitudinal variability.

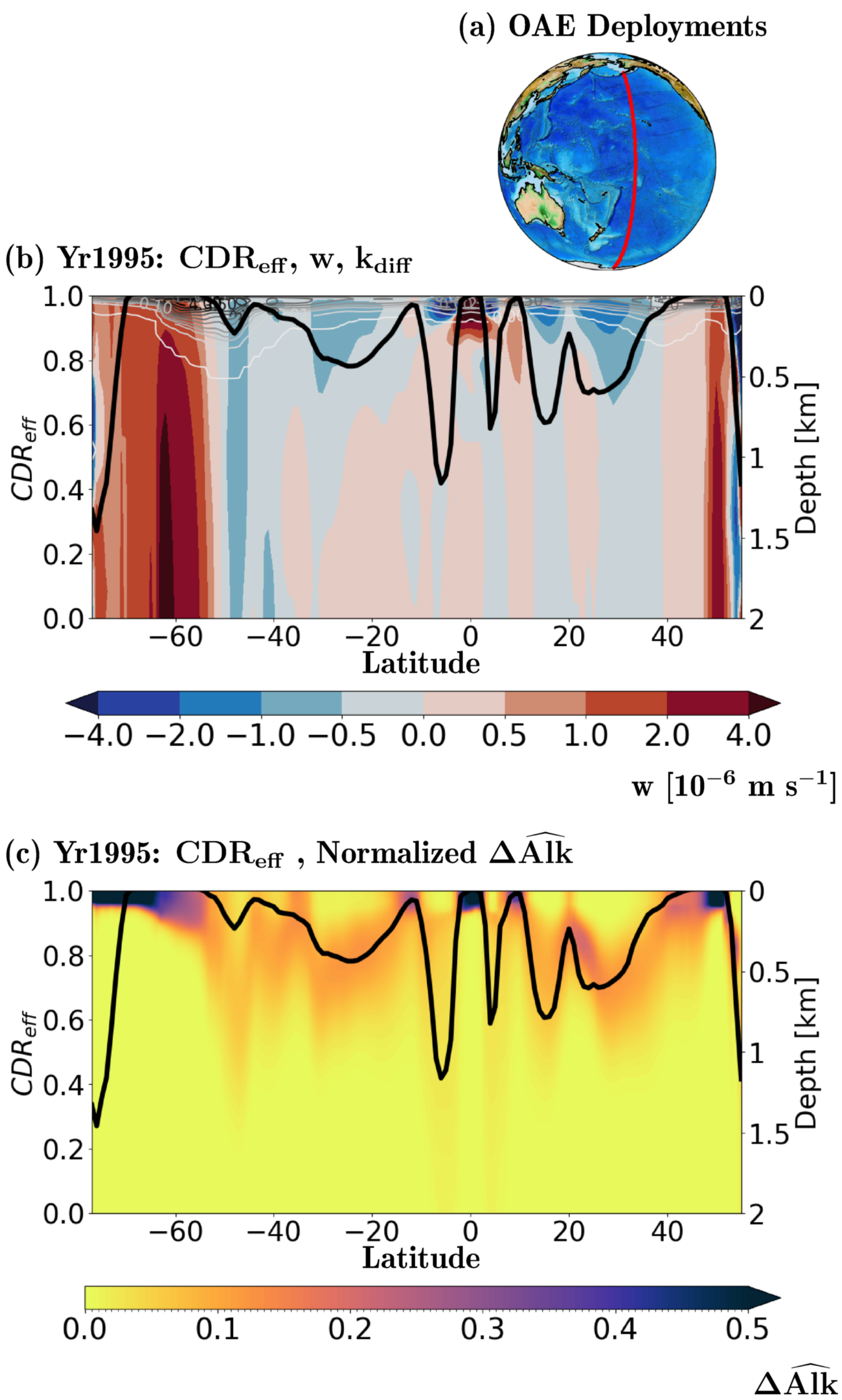

Figure 11. (a) Location of rapid-mCDR deployment sites across the Pacific Ocean; (b) $mCDR_{eff}$ at the end of 2017 for Yr1995 experiment (solid black line), profile of mean vertical velocity (colored contours), and vertical diffusivity (grayscale contour lines with units of 10^{-2} m^2 s^{-1}); (c) $mCDR_{eff}$ at the end of 2017 for Yr1995 experiment (solid black line) and normalized $\Delta\widehat{Alk}$ (colored contours).

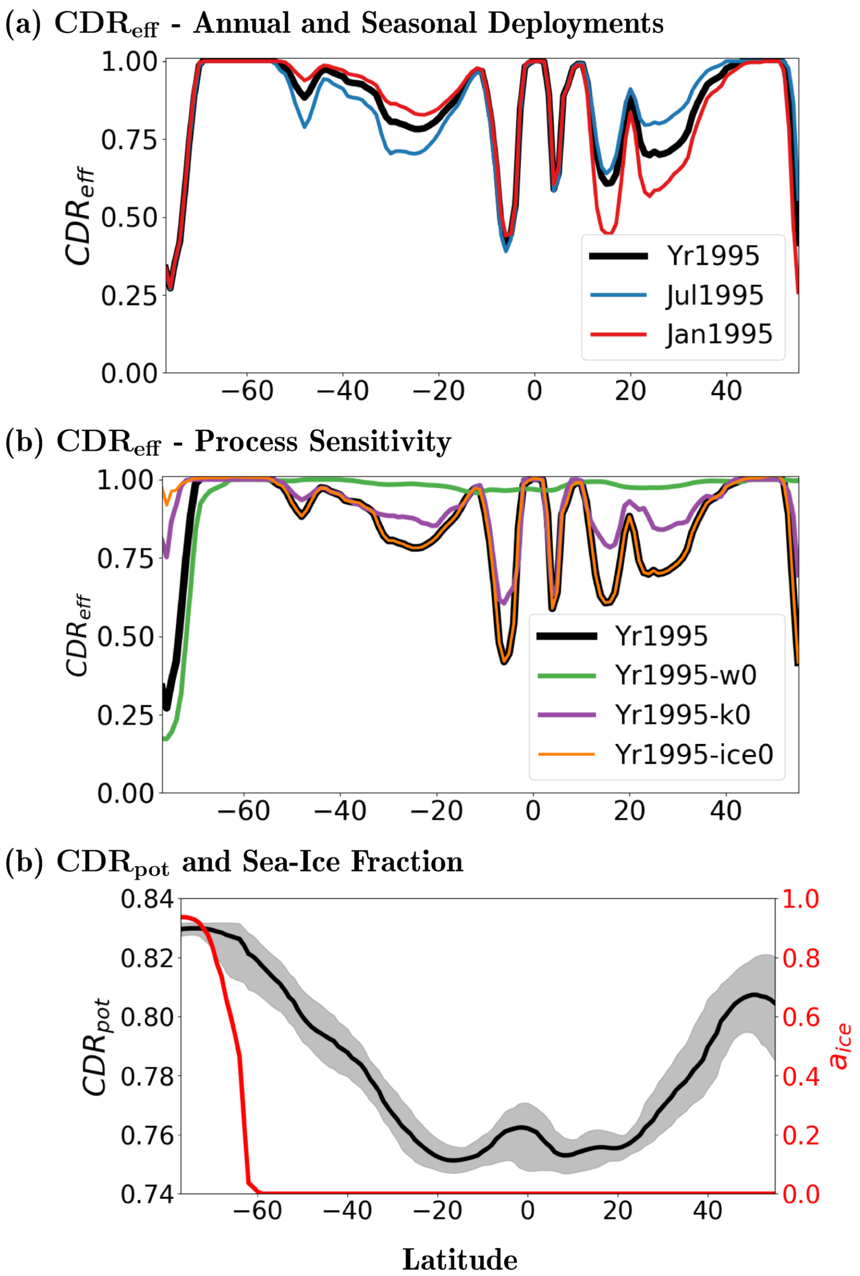

Figure 12. Pacific Ocean vertical sections of $mCDR_{eff}$ at the end of 2017 for (a) 3 different pulse deployment seasons (Jul1995, Jan1995, and Yr1995). (b) Experiment with vertical velocity and diffusivity set to zero (Yr1995-w0 and Yr1995-k0, respectively) and simulation without sea ice forcing (Yr1995-ice0). (c) Mean $mCDR_{pot}$and variability over the deployment site (solid black lines and gray shading, respectively); these are computed from daily-mean values and time-mean sea-ice cover. All values are shown at the central latitude of the deployment site.

5 Discussion

In recent years, mCDR efforts via OAE have gathered considerable attention as a potential method for removing anthropogenic CO_2 from the atmosphere. The OAE approach mimics natural processes (Subhas et al., 2023) and has a potential to be scaled-up to significantly mitigate climate change (Renforth & Henderson, 2017). As the efficiency of OAE-based mCDR varies across different spatial and temporal scales, field deployments must be carefully planned to achieve maximum efficiency while minimizing cost and logistical risk. While a number of field methods, technical approaches, and experiment designs have been proposed (Eisaman et al., 2023), the use of numerical ocean models to simulate and quantify OAE impacts before expensive field trials occur, and provide much-needed MRV quantification (Ho et al., 2023), still remains in its infancy.

While experiments and observations (Boyd et al., 2023) will be invaluable to inform these efforts, environmentally- and societally-responsible OAE perturbations (Fakhraee et al., 2022; Nawaz et al., 2023) should modify the natural ocean carbonate and ecological state (Ferderer et al., 2022) only slightly compared to its natural variability. Our work shows that the impacts of OAE are spatially dispersed across ocean basins before the full CO_2 potential is realized. Due to these two factors, it will be difficult if not impossible to observe and separate actual OAE-deployment effects from natural ocean variability. Therefore, the optimization of deployment strategies and their MRV will have to heavily rely on numerical models. Numerical models are also the ideal tool for exploring and quantifying efficiencies of potential mCDR deployment strategies before significant investments in deployment infrastructure occur.

In this paper, we use a state-of-the-art ocean biogeochemistry state estimate (ECCO-Darwin) constrained by a suite of in-situ and remotely-sensed observations, to quantify OAE additionality and to characterize the resultant 3-D ocean carbonate state perturbation attributed to regional-scale, multi-decadal 1) continuous and 2) month- and year-long surface-ocean Alk deployment. To our knowledge, ECCO-Darwin is the only open-source model at present time that is ideally suited for attribution of the ocean physical-sea-ice-biogeochemical state and OAE additionality. This is because of its unique data assimilation approach, which is a combination of adjoint-based (Wunsch et al., 2009; Wunsch & Heimbach, 2013) and Green's function (Menemenlis et al., 2005) approaches that constrains the dynamical, carbonate, and biogeochemical state with a suite of observations (Carroll et al., 2022). Thus ECCO-Darwin provides an accurate background state, and in particular, 3-D ocean physics, for studying the impact of mCDR over multi-decadal timescales. Furthermore, the data assimilation in ECCO-Darwin does not introduce non-physical observation-based nudging or increments which can conceal the impact of OAE.

The alternative approaches include forward-only ocean-biogeochemistry models unconstrained by observations. These models typically exhibit larger biases in terms of ocean dynamics and carbonate cycle (e.g., Séférian et al., 2020; Fu et al., 2022) compared to the ECCO-Darwin solution described in Carroll et al. (2020, 2022). These model biases are expected to contribute to additional uncertainty and biases in ocean CO_2 solubility and dynamics, which are both important considerations for mCDR studies. Modeling systems that assimilate either one or all of the components of the ocean system (e.g., Perruche, 2018; Turner et al., 2023) are usually based on sequential data assimilation and correct simulated fields with observational increment. These data assimilation systems are geared towards the best representation of the ocean state, but conceal relationship between processes which introduces uncertainties in attribution studies, for example attribution of OAE additionality.

Furthermore, we use our numerical ocean model results to motivate and develop a 1-D model for rapid quantification of OAE additionality (rapid-mCDR). Rapid-mCDR provides a user friendly and easily-deployable model for mCDR end-users that can be used across various ocean conditions without the need for supercomputing resources — which is a key advantage compared to more-complex ECCO-Darwin simulations. Combining the 1-D model approach with output from a numerical ocean biogeochemistry model, such as ECCO-Darwin, permits rapid characterization of mCDR additionality at any location in the global-ocean model grid, which can be a backbone for MRV purposes, as well as a tool for rapid comparison and optimization of different OAE deployment strategies. All of our experiments represent open-ocean deployments (rather than coastal sites). We are aware that many planned OAE field deployments will occur in coastal regions or from the nearshore zone, which might require additional model improvements and features.

Similar to Wang et al., 2023, we separate mCDR efficiency into two factors controlling: 1) CO_2 solubility (mCDR potential, $mCDR_{pot}$; the maximum amount of CO_2 that can be sequestered per deployed Alk), and 2) dynamical efficiency ($mCDR_{eff}$; a nondimensional function that represents a fraction of realized $mCDR_{pot}$ with the time after deployment, which is dominated by ocean dynamics and sea-ice cover). We characterize $mCDR_{pot}$ globally from two independent data sources, the 1) baseline ECCO-Darwin simulation and 2) OceanSODA-ETHZ dataset. The $mCDR_{pot}$ from both datasets shows similar features, including:

- Meridional dependence dominated by increase of CO_2 solubility with colder SSTs. This indicates that in the absence of dynamical effects, near-polar regions would be associated with the highest potential for CO_2 removal.
- Weaker dependence within the ocean basins dominated by meridional transport and vertical mixing associated with basin-scale boundary currents, river inflows, and sea-ice melt which impact the saturated surface-ocean CO_2 state.
- Seasonal variability is small for most regions; the highest seasonal variability is found in the mid-latitudinal regions and particularly in western boundary currents.
- Despite substantial secular trends in CO_2 uptake (Carroll et al., 2020), the linear trend of $mCDR_{pot}$ remains below 0.01 mol C/mol Alk per decade, with minimal interannual variability. We expect an overall decrease of $mCDR_{pot}$ in the future climate due to ocean warming and accelerated acidification.

Compared to mCDR potential, evaluation of dynamical mCDR efficiency using ECCO-Darwin is computationally intensive – for each considered OAE deployment, a multi-decadal ECCO-Darwin simulation is run and $mCDR_{eff}$ is computed from the additionality of CO_2 uptake with respect to the baseline simulation.

We find that OAE simulations with continuous Alk deployment are well suited for a general characterization of regional mCDR efficiency, as these simulations can also provide information on the seasonal cycle of OAE-induced CO_2 uptake. Locations associated with large seasonality are likely to exhibit sensitivity in $mCDR_{eff}$ depending on the deployment season, which can be further quantified with targeted short-term (pulse) experiments. The main feature of dynamical mCDR efficiency are:

- Regional-scale ocean circulation, and in particular vertical transport, exerts a strong control on the space-time distribution of $mCDR_{eff}$ and taken together with $mCDR_{pot}$ are the first-order control on sequestration efficiency of OAE-induced atmospheric CO_2 to depth.

- Downwelling/subduction regions are associated with low values of $mCDR_{eff}$ and upwelling regions exhibit high $mCDR_{eff}$ — this is because of the relatively long timescales of ocean-atmosphere CO_2 equilibration (on the order of years) which takes place against the backdrop of shorter-scale ocean dynamics which can isolate CO_2 from non-equilibrated waters from the atmosphere.
- In high-latitude regions, sea-ice cover can strongly reduce $mCDR_{eff}$ due to blocking of air-sea gas exchange.
- For extratropical deployments, $mCDR_{eff}$ can be heavily dependent on the deployment season — summer is generally associated with higher values.
- Multi-annual variability in $mCDR_{eff}$ is found for all deployment sites, and is particularly significant in the Tropical and Equatorial Pacific Ocean.
- For most of the studied deployments, OAE-impacted waters remain above 500 m depth for the duration of the 27-year long continuous experiments. The exception to this is NAS, in which the OAE perturbation reaches below 1000 m within roughly four years and eventually penetrates below 2000 m.

We stress that care must be taken when relating the seasonal cycle of dynamical efficiency from continuous OAE experiments to the most efficient deployment season, as these are not the same. The seasonal efficiency from continuous OAE experiments indicates the seasonality of OAE additionality with the most-efficient deployment time often being a few months prior to the season with the highest CO_2 uptake.

One of our deployment sites, NAS, is very close to the Iceland pulse experiment from (He & Tyka, 2023), for which they find a much lower efficiency compared to their other locations. Our experiments indicate that the time-mean mCDR efficiency of that location is comparable to the other sites examined in this study. The NAS location is however associated with large seasonal variability of mCDR efficiency, with very low values during winter for which the deployment in (He & Tyka, 2023) was performed. Therefore, our results largely agree with (He & Tyka, 2023) and we further show that their results are heavily influenced by the seasonal cycle of mCDR efficiency.

We find that the 1-D model rapid-mCDR can rapidly and realistically reproduce OAE simulations performed with a complete 3-D ocean biogeochemistry model. Futhermore, rapid-mCDR can be used to isolate and compare the individual processes that drive mCDR efficiency and thus provides additional benefits in terms of improving the physical understanding of mechanisms that control mCDR efficiency. The rapid-mCDR inputs are horizontal mean fields from the baseline ECCO-Darwin simulation, which provides a background information on the ocean state that is affected by OAE. We test two approaches with respect to the horizontal averaging method: 1) ocean fields are spatial means over the deployment site — the results of this approach neglect horizontal advection of the OAE perturbation and 2) Surface-ocean advection is included and used to advect the OAE perturbation throughout the water column. We refer to the two approaches as rapid-mCDR (Deploy) and rapid-mCDR (HorAdv), respectively.

The key findings using rapid-mCDR are:

- We find good agreement with ECCO-Darwin in extratropical regions, especially when the horizontal advection is considered.
- For tropical regions, interannual variability is poorly represented, especially for the rapid-mCDR simulation which neglects horizontal advection. We note that including horizontal advection improves its representation, although there is still room for improvement. We speculate that the horizontal advection of OAE perturbation and strong spatial gradients in ocean dynamics surrounding the EU deployment site play an important role in controlling $mCDR_{eff}$, which can only be crudely represented by the 1-D rapid-mCDR model.
- Ocean vertical velocity dominates over vertical diffusivity in its control on $mCDR_{eff}$. In high-latitudes, seasonal sea-ice cover can significantly decrease $mCDR_{eff}$.

5.1 Future Model Improvements

The ECCO-Darwin experiments shown in this work are idealized and we assume that surface-ocean Alk rate is known without consideration of a specific deployment method. Therefore, we suggest that future work tailoring numerical ocean simulations towards more-realistic deployment strategies might include:

- Improved parameterization of interactions between the OAE material and seawater to represent relevant processes for the particular deployment strategy and might include mineral dissolution and precipitation (e.g., Fennel et al., 2023).
- Simulation of deployment via minerals and dissolution products, such as Si and Fe, which might interact with ocean biota (Bach et al., 2019). While there is un-

certainty in understanding of the response of major phytoplantkton types to increased Alk (e.g., Gately et al., 2023), ECCO-Darwin is well suited to account for dispersion of these products as the Darwin component can simulate their impact on key plankton functional types.

- In the current version of ECCO-Darwin, air-sea CO_2 flux in seasonally ice-covered regions is simplified — with CO_2 flux being scaled by the fraction of open-water area, i.e., 1 - sea-ice cover. Future work should account for a realistic representation of air-sea gas exchange through sea-ice cracks and leads (Loose & Schlosser, 2011; Søren et al., 2011).
- Developing regional downscaled set-ups of ECCO-Darwin on higher-resolution grids, or incorporation of unstructured grids in nearshore mCDR simulations (Ward et al., 2020), to improve resolution and representation of the coastal periphery and topography in the desired region. This will provide a better representation of ocean dynamics and help resolve small-scale coastal flows, which may be important for coastally-based deployment strategies.

We envision that rapid-mCDR will continue to be a useful tool for quick and efficient evaluation of potential OAE deployments or as the backbone for MRV. Future improvements to rapid-mCDR might include:

- Improved representation of horizontal advection and dispersion of OAE-impacted seawater. The rapid-mCDR simulations at all 5 deployment regions demonstrate improvements in terms of fit to ECCO-Darwin when surface-ocean advection is considered. We note that this improvement is particularly significant for tropical regions (EU). We suggest that two possible approaches could be used to improve rapid-mCDR accuracy in this regard: 1) an Eulerian approach where surface advection is estimated using an offline calculation, for example with OceanPARCELS (Lange & van Sebille, 2017; Delandmeter & van Sebille, 2019) and 2) a Lagrangian approach where rapid-mCDR is coupled to a particle tracking model and solved at each point along the dispersal trajectory. This could be used to estimate the transport, sinking, and dissolution of minerals added to the surface ocean and inform regional-scale Eulerian ocean model simulations.
- Improving representation of bathymetry and its impact on the spread of OAE-impacted waters. The current version of rapid-mCDR is developed for the deep ocean and

we assume that the OAE impact does not spread to the seafloor. At the seafloor, rapid-mCDR could be coupled with a sediment diagenesis model, such as RADI (Sulpis et al., 2021), to account for sequestration of particulate carbon in sediment and the resultant fluxes between porewaters and the overlying seawater.

- Parameterization of biogeochemical processes to tailor rapid-mCDR for other mCDR approaches, e.g., ocean afforestation/macroalgage growth, iron-fertilization, and enhanced phytoplankton growth.
- Implement a module for uncertainty quantification of mCDR impact using a Monte-Carlo/ensemble approach.

6 Summary and Conclusions

Using a data-assimilative ocean biogeochemistry model (ECCO-Darwin), we have characterized the regional-scale efficiency of OAE additionality over seasonal to multi-decadal timescales. Using both pulsed and continuous OAE experiments at five distinct open-ocean deployment sites, this work highlights the strong role of three-dimensional ocean dynamics in transporting OAE-induced atmospheric carbon across ocean basins and to depth. We also develop a 1-D model approach (rapid-mCDR) that can be run on a personal computer to rapidly characterize OAE efficiency at any global-ocean location, with a single multi-decadal simulation taking only about 1 CPU minute. Rapid-mCDR can be readily expanded to other mCDR approaches, such as ocean afforestation and iron fertilization. Our foundational data-constrained modeling work provides a path forward for quantifying the global-ocean response to OAE deployments and can be used to develop high-resolution downscaled OAE simulations to complement and support future mCDR field trials.

Open Research Section

ECCO-Darwin model output is available at the ECCO Data Portal: `http://data.nas.nasa.gov/ecco/`

Model code and platform-independent instructions for running ECCO-Darwin and rapid-mCDR simulations are available at: https://doi.org/10.5281/zenodo.10562714

Acknowledgments

A portion of this research was carried out at the Jet Propulsion Laboratory, California Institute of Technology, under a contract with the National Aeronautics and Space Administration (80NM0018D0004). Support from the Carbon Cycle Science (CCS) and Carbon Monitoring Systems (CMS) programs are acknowledged. High-end computing resources were provided by the NASA Advanced Supercomputing (NAS) Division of the Ames Research Center. Government sponsorship acknowledged.

References

Andrews, A. E., Kofler, J. D., Trudeau, M. E., Williams, J. C., Neff, D. H., Masarie, K. A., ... Tans, P. P. (2014). CO_2, CO, and CH_4 measurements from tall towers in the NOAA Earth System Research Laboratory's Global Greenhouse Gas Reference Network: instrumentation, uncertainty analysis, and recommendations for future high-accuracy greenhouse gas monitoring efforts. *Atmospheric Measurement Techniques*, *7*(2), 647–687.

Bach, L. T., Gill, S. J., Rickaby, R. E. M., Gore, S., & Renforth, P. (2019). Co2 removal with enhanced weathering and ocean alkalinity enhancement: Potential risks and co-benefits for marine pelagic ecosystems. *Frontiers in Climate*, *1*.

Bertin, C., Carroll, D., Menemenlis, D., Dutkiewicz, S., Zhang, H., Matsuoka, A., ... Le Fouest, V. (2023). Biogeochemical River Runoff Drives Intense Coastal Arctic Ocean CO2 Outgassing. *Geophysical Research Letters*, *50*(8), e2022GL102377. doi: 10.1029/2022GL102377

Boyd, P. W., Claustre, H., Legendre, L., Gattuso, J.-P., & Traon, P.-Y. L. (2023). Operational monitoring of open-ocean carbon dioxide removal deployments: Detection, attribution, and determination of side effects. *Oceanography*, *36*(1), 2–10.

Brix, H., Menemenlis, D., Hill, C. N., Dutkiewicz, S., Jahn, O., Wang, D., ... Zhang, H. (2015). Using Green's Functions to initialize and adjust a global, eddying ocean biogeochemistry general circulation model. *Ocean Modelling*, *95*, 1–14.

Burt, D. J., Fröb, F., & Ilyina, T. (2021). The sensitivity of the marine carbonate system to regional ocean alkalinity enhancement. *Frontiers in Climate*, *3*.

Carroll, D., Menemenlis, D., Adkins, J. F., Bowman, K. W., Brix, H., Dutkiewicz, S., ... Zhang, H. (2020). The ECCO-Darwin Data-Assimilative Global Ocean Biogeochemistry Model: Estimates of Seasonal to Multidecadal Surface Ocean p CO_2 and Air-Sea CO_2 Flux. *Journal of Advances in Modeling Earth Systems*, *12*(10), 1–28.

Carroll, D., Menemenlis, D., Dutkiewicz, S., Lauderdale, J. M., Adkins, J. F., Bowman, K. W., ... Zhang, H. (2022). Attribution of space-time variability in global-ocean dissolved inorganic carbon. *Global Biogeochemical Cycles*, *36*(3), e2021GB007162.

Delandmeter, P., & van Sebille, E. (2019). The Parcels v2.0 Lagrangian framework: new field interpolation schemes. *Geoscientific Model Development*, *12*(8), 3571–3584. doi: 10.5194/gmd-12-3571-2019

Dutkiewicz, S., Cermeno, P., Jahn, O., Follows, M. J., Hickman, A. E., Taniguchi, D. A. A., & Ward, B. A. (2020). Dimensions of marine phytoplankton diversity. *Biogeosciences*, *17*(3), 609–634.

Dutkiewicz, S., Hickman, A. E., Jahn, O., Gregg, W. W., Mouw, C. B., & Follows, M. J. (2015). Capturing optically important constituents and properties in a marine biogeochemical and ecosystem model. *Biogeosciences*, *12*(14), 4447–4481.

ECCO Consortium. (2021). *Synopsis of the ECCO Central Production Global Ocean and Sea-Ice State Estimate, Version 4 Release 4.* Zenodo. doi: 10.5281/zenodo.4533349

Eisaman, M. D., Geilert, S., Renforth, P., Bastianini, L., Campbell, J., Dale, A. W., ... Rønning, J. (2023). Assessing the technical aspects of ocean-alkalinity-enhancement approaches. *State of the Planet*, *2-oae2023*, 3.

Fakhraee, M., Li, Z., Planavsky, N., & Reinhard, C. (2022). *Environmental impacts and carbon capture potential of ocean alkalinity enhancement.* Research Square. Retrieved from `https://doi.org/10.21203/rs.3.rs-1475007/v1` doi: 10.21203/rs.3.rs-1475007/v1

Fennel, K., Long, M. C., Algar, C., Carter, B., Keller, D., Laurent, A., ... Whitt, D. B. (2023). *Modeling considerations for research on Ocean Alkalinity Enhancement (OAE)* (preprint). doi: 10.5194/sp-2023-10

Ferderer, A., Chase, Z., Kennedy, F., Schulz, K. G., & Bach, L. T. (2022). Assessing the influence of ocean alkalinity enhancement on a coastal phytoplankton community. *Biogeosciences*, *19*(23), 5375–5399.

Follows, M. J., Dutkiewicz, S., Grant, S., & Chisholm, S. W. (2007). Emergent Biogeography of Microbial Communities in a Model Ocean. *Science*, *315*(5820), 1843–1846.

Follows, M. J., Ito, T., & Dutkiewicz, S. (2006). On the solution of the carbonate chemistry system in ocean biogeochemistry models. *Ocean Modelling*, *12*(3), 290–301.

Forget, G., Campin, J.-M., Heimbach, P., Hill, C. N., Ponte, R. M., & Wunsch, C. (2015). ECCO version 4: an integrated framework for non-linear inverse modeling and global ocean state estimation. *Geoscientific Model Development*, *8*(10), 3071–3104.

Friedlingstein, P., Jones, M. W., O'Sullivan, M., Andrew, R. M., Bakker, D. C. E., Hauck, J., ... Zeng, J. (2022). Global carbon budget 2021. *Earth System Science Data*, *14*(4), 1917–2005.

Fu, W., Moore, J. K., Primeau, F., Collier, N., Ogunro, O. O., Hoffman, F. M., & Randerson, J. T. (2022). Evaluation of Ocean Biogeochemistry and Carbon Cycling in CMIP Earth System Models With the International Ocean Model Benchmarking (IOMB) Software System. *Journal of Geophysical Research: Oceans*, *127*(10), e2022JC018965. doi: 10.1029/2022JC018965

Gaspar, P., Grégoris, Y., & Lefevre, J.-M. (1990). A simple eddy kinetic energy model for simulations of the oceanic vertical mixing: Tests at station papa and long-term upper ocean study site. *Journal of Geophysical Research: Oceans*, *95*(C9), 16179-16193.

Gately, J. A., Kim, S. M., Jin, B., Brzezinski, M. A., & Iglesias-Rodriguez, M. D. (2023). Coccolithophores and diatoms resilient to ocean alkalinity enhancement: A glimpse of hope? *Science Advances*, *9*(24), eadg6066. doi: 10.1126/sciadv.adg6066

Gent, P. R., & McWilliams, J. C. (1990). Isopycnal mixing in ocean circulation models. *Journal of Physical Oceanography*, *20*(1), 150–155.

González, M. F., Ilyina, T., Sonntag, S., & Schmidt, H. (2018). Enhanced rates of regional warming and ocean acidification after termination of large-scale ocean alkalinization. *Geophysical Research Letters*, *45*(14), 7120–7129.

Gregor, L., & Gruber, N. (2021). Oceansoda-ethz: a global gridded data set of the surface ocean carbonate system for seasonal to decadal studies of ocean acidification. *Earth System Science Data*, *13*(2), 777–808.

Gruber, N., Clement, D., Carter, B. R., Feely, R. A., van Heuven, S., Hoppema, M., ... Wanninkhof, R. (2019). The oceanic sink for anthropogenic co_2 from 1994 to 2007. *Science*, *363*(6432), 1193–1199.

He, J., & Tyka, M. D. (2023). Limits and CO $_2$ equilibration of near-coast alkalinity enhancement. *Biogeosciences*, *20*, 27–43.

Ho, D. T., Bopp, L., Palter, J. B., Long, M. C., Boyd, P. W., Neukermans, G., & Bach, L. T. (2023). Monitoring, reporting, and verification for ocean alkalinity enhancement. *State of the Planet*, *2-oae2023*, 12.

House, K. Z., House, C. H., Schrag, D. P., & Aziz, M. J. (2007). Electrochemical acceleration of chemical weathering as an energetically feasible approach to mitigating anthropogenic climate change. *Environmental Science & Technology*, *41*(24), 8464-8470. doi: 10.1021/es0701816

Humphreys, M. P., Lewis, E. R., Sharp, J. D., & Pierrot, D. (2022). PyCO2SYS v1.8: marine carbonate system calculations in Python. *Geoscientific Model Development*, *15*(1), 15–43.

Iglesias-Rodríguez, M. D., Rickaby, R. E. M., Singh, A., & Gately, J. A. (2023). Laboratory experiments in ocean alkalinity enhancement research. *State of the Planet*, *2-oae2023*, 5.

Ilyina, T., Wolf-Gladrow, D., Munhoven, G., & Heinze, C. (2013). Assessing the potential of calcium-based artificial ocean alkalinization to mitigate rising atmospheric CO_2 and ocean acidification. *Geophysical Research Letters*, *40*(22), 5909–5914.

IPCC. (2022). *Climate change 2022: Mitigation of climate change. contribution of working group iii to the sixth assessment report of the intergovernmental panel on climate change* (P. Shukla et al., Eds.). Cambridge, UK and New York, NY, USA: Cambridge University Press. doi: 10.1017/9781009157926

Jo, A. R., Lee, J., Timmermann, A., Jin, F., Yamaguchi, R., & Gallego, A. (2022). Future amplification of sea surface temperature seasonality due to enhanced ocean stratification. *Geophysical Research Letters*, *49*(9), e2022GL098607.

Jones, D. C., Ito, T., Takano, Y., & Hsu, W.-C. (2014). Spatial and seasonal variability of the air-sea equilibration timescale of carbon dioxide. *Global Biogeo-*

chemical Cycles, *28*(11), 1163–1178.

Köhler, P., Abrams, J. F., Völker, C., Hauck, J., & Wolf-Gladrow, D. A. (2013). Geoengineering impact of open ocean dissolution of olivine on atmospheric co2, surface ocean ph and marine biology. *Environmental Research Letters*, *8*(1), 014009.

Lange, M., & van Sebille, E. (2017). Parcels v0.9: prototyping a Lagrangian ocean analysis framework for the petascale age. *Geoscientific Model Development*, *10*(11), 4175–4186. doi: 10.5194/gmd-10-4175-2017

Loose, B., & Schlosser, P. (2011). Sea ice and its effect on CO2 flux between the atmosphere and the Southern Ocean interior. *Journal of Geophysical Research: Oceans*, *116*(C11). doi: 10.1029/2010JC006509

Manizza, M., Carroll, D., Menemenlis, D., Zhang, H., & Miller, C. E. (2023). Modeling the Recent Changes of Phytoplankton Blooms Dynamics in the Arctic Ocean. *Journal of Geophysical Research: Oceans*, *128*(6), e2022JC019152. doi: 10.1029/2022JC019152

Manizza, M., Menemenlis, D., Zhang, H., & Miller, C. E. (2019, mar). Modeling the Recent Changes in the Arctic Ocean CO_2 Sink (2006–2013). *Global Biogeochemical Cycles*, *33*(3), 420–438.

Menemenlis, D., Fukumori, I., & Lee, T. (2005). Using Green's Functions to Calibrate an Ocean General Circulation Model. *Monthly Weather Review*, *133*(5), 1224–1240.

Middelburg, J. J., Soetaert, K., & Hagens, M. (2020). Ocean alkalinity, buffering and biogeochemical processes. *Reviews of Geophysics*, *58*(3), e2019RG000681.

Montserrat, F., Renforth, P., Hartmann, J., Leermakers, M., Knops, P., & Meysman, F. J. R. (2017). Olivine Dissolution in Seawater: Implications for CO $_2$ Sequestration through Enhanced Weathering in Coastal Environments. *Environ. Sci. Technol.*(7), 3960–3972.

National Academies of Sciences, Engineering, and Medicine. (2022). *A Research Strategy for Ocean-based Carbon Dioxide Removal and Sequestration.* Washington, DC: The National Academies Press. doi: 10.17226/26278

Nawaz, S., Lezaun, J., Valenzuela, J. M., & Renforth, P. (2023). Broaden research on ocean alkalinity enhancement to better characterize social impacts. *Environmental Science & Technology*, *57*(24), 8863-8869.

Palter, J., Cross, J., Long, M., Rafter, P., & Reimers, C. (2023). The science we need to assess marine carbon dioxide removal. *Eos*, *104*.

Perruche, C. (2018). *Product User Manual for the Global Ocean Biogeochemistry Hindcast GLOBAL_reanalysis_bio_001_029. Version 1.* (Report). Copernicus Marine Environment Monitoring Service. Retrieved from https://repository.oceanbestpractices.org/handle/11329/955 doi: 10.25607/OBP-490

Redi, M. H. (1982). Oceanic isopycnal mixing by coordinate rotation. *Journal of Physical Oceanography*, *12*(10), 1154–1158.

Renforth, P., & Henderson, G. (2017). Assessing ocean alkalinity for carbon sequestration. *Reviews of Geophysics*, *55*(3), 636-674.

Rogelj, J., Popp, A., Calvin, K. V., Luderer, G., Emmerling, J., Gernaat, D., ... Tavoni, M. (2018). Scenarios towards limiting global mean temperature increase below 1.5^{circ}c. *Nature Climate Change*, *8*(4), 325–332.

Sarmiento, J., & Gruber, N. (2006). *Ocean biogeochemical dynamics.* Princeton University Press.

Schimel, D. S., & Carroll, D. (2024). Carbon cycle–climate feedbacks in the post-paris world. *Annual Review of Earth and Planetary Sciences*, *52*(1), null. doi: 10.1146/annurev-earth-031621-081700

Subhas, A. V., Lehmann, N., & Rickaby, R. E. M. (2023). Natural analogs to ocean alkalinity enhancement. *State of the Planet*, *2-oae2023*, 8.

Sulpis, O., Humphreys, M., Wilhelmus, M., Carroll, D., Berelson, W., Menemenlis, D., ... Adkins, J. (2021). Radiv1: a non-steady-state early diagenetic model for ocean sediments in julia and matlab/gnu octave. *Geoscientific Model Development Discussions*, *2021*, 1–41. Retrieved from https://gmd.copernicus.org/preprints/gmd-2021-211/ doi: 10.5194/gmd-2021-211

Séférian, R., Berthet, S., Yool, A., Palmiéri, J., Bopp, L., Tagliabue, A., ... Yamamoto, A. (2020). Tracking Improvement in Simulated Marine Biogeochemistry Between CMIP5 and CMIP6. *Curr Clim Change Rep*, *6*(3), 95–119. doi: 10.1007/s40641-020-00160-0

Søren, R., Bendtsen, J., Delille, B., Dieckmann, G. S., Glud, R. N., Kennedy, H., ... Tison, J.-L. (2011). Sea ice contribution to the air–sea CO2 exchange in the

Arctic and Southern Oceans. *Tellus B: Chemical and Physical Meteorology*, *63*(5), 823–830. doi: 10.1111/j.1600-0889.2011.00571.x

Taylor, L. L., Quirk, J., Thorley, R. M. S., Kharecha, P. A., Hansen, J., Ridgwell, A., … Beerling, D. J. (2016). Enhanced weathering strategies for stabilizing climate and averting ocean acidification. *Nature Clim Change*, *6*, 402–406.

Turner, K. E., Smith, D. M., Katavouta, A., & Williams, R. G. (2023). Reconstructing ocean carbon storage with CMIP6 Earth system models and synthetic Argo observations. *Biogeosciences*, *20*(8), 1671–1690. doi: 10.5194/bg-20-1671-2023

Tyka, M. D., Van Arsdale, C., & Platt, J. C. (2022). CO $_2$ capture by pumping surface acidity to the deep ocean. *Energy Environ. Sci.*, *15*(2), 786–798. Retrieved 2023-08-03, from `http://xlink.rsc.org/?DOI=D1EE01532J` doi: 10.1039/D1EE01532J

Wang, H., Pilcher, D. J., Kearney, K. A., Cross, J. N., Shugart, O. M., Eisaman, M. D., & Carter, B. R. (2023). Simulated impact of ocean alkalinity enhancement on atmospheric CO_2 removal in the bering sea. *Earth's Future*, *11*(1), e2022EF002816.

Wanninkhof, R. (1992). Relationship between wind speed and gas exchange over the ocean. *Journal of Geophysical Research: Oceans*, *97*(C5), 7373–7382.

Ward, N. D., Megonigal, J. P., Bond-Lamberty, B., Bailey, V. L., Butman, D., Canuel, E. A., … Windham-Myers, L. (2020). Representing the function and sensitivity of coastal interfaces in earth system models. *Nature Communications*, *11*(1), 2458.

Wolter, K., & Timlin, M. S. (2011). El Niño/Southern Oscillation behaviour since 1871 as diagnosed in an extended multivariate ENSO index (MEI.ext). *International Journal of Climatology*, *31*(7), 1074–1087. doi: 10.1002/joc.2336

Wunsch, C., & Heimbach, P. (2013). Dynamically and kinematically consistent global ocean circulation and ice state estimates. In G. Siedler, S. M. Griffies, J. Gould, & J. A. Church (Eds.), *Ocean circ. clim. a 21st century perspect.* (Vol. 103, pp. 553–579). New York, NY: Academic Press.

Wunsch, C., Heimbach, P., Ponte, R., & Fukumori, I. (2009). The Global General Circulation of the Ocean Estimated by the ECCO-Consortium. *Oceanography*, *22*(2), 88–103.

Zeebe, R. E., & Wolf-Gladrow, D. (2001). *Co_2 in seawater: equilibrium, kinetics, isotopes* (No. 65). Gulf Professional Publishing.